Sequential Transitions of Male Sexual Behaviours Driven by Dual Acetylcholine-Dopamine Dynamics

Ai Miyasaka[1,2], Takeshi Kanda[1,3#], Naoki Nonaka[2#], Yuka Terakoshi[1], Yoan Cherasse[1], Yukiko Ishikawa[1], Yulong Li[4], Hotaka Takizawa[5,6], Jun Seita[2], Masashi Yanagisawa[1,7,8], Takeshi Sakurai[1,9,10*], Katsuyasu Sakurai[1*], Qinghua Liu[1,11,12*]

[1]International Institute for Integrative Sleep Medicine, University of Tsukuba, Tsukuba, Ibaraki 305-8575, Japan.

[2]Advanced Data Science Project, RIKEN Information R&D and Strategy Headquarters, RIKEN, Tokyo 103-0027, Japan.

[3]Department of Neurophysiology, Nara Medical University, Kashihara, Nara 634-8521, Japan

[4]State Key Laboratory of Membrane Biology, Peking University School of Life Sciences, Beijing 100871, China.

[5]Institute of Systems and Information Engineering, University of Tsukuba, Tsukuba, Ibaraki 305-8573, Japan.

[6]Academic Computing and Communications Center, University of Tsukuba, Tsukuba, Ibaraki 305-8577, Japan.

[7]Department of Molecular Genetics, University of Texas Southwestern Medical Center, Dallas, TX 75390, USA

[8]Life Science Center for Survival Dynamics, Tsukuba Advanced Research Alliance, University of Tsukuba, Tsukuba, Ibaraki 305-8575, Japan

[9]Institute of Medicine, University of Tsukuba, Tsukuba, Ibaraki 305-8575, Japan.

[10]Life Science Center for Tsukuba Advanced Research Alliance (TARA), University of Tsukuba, Tsukuba, Ibaraki 305-8575, Japan.

[11]National Institute of Biological Sciences, Beijing (NIBS), Beijing 102206, China.

[12]Tsinghua Institute of Multidisciplinary Biomedical Research (TIMBR), Tsinghua University, Beijing 102206, China.

[#]These authors contributed equally to this work

[*]Correspondence: sakurai.takeshi.gf@u.tsukuba.ac.jp

sakurai.katsuyasu.gm@u.tsukuba.ac.jp

liuqinghua@nibs.ac.cn

Abstract

In mammals, males execute a stereotypical and organized sequence of sexual behaviours, such as mounting, intromission, and ejaculation, to successfully complete copulation. However, the neural mechanisms that govern the sequential transitions of male copulatory behaviours remain unclear. Here, we report that dopamine (DA) and acetylcholine (ACh) dynamics in the ventral shell of the nucleus accumbens (vsNAc) closely align with serial transitions of sexual behaviours in male mice. In particular, the vsNAc exhibits a unique pattern of 1.5–2.2 Hz dual ACh-DA rhythms that correspond to the pelvic thrust rhythm during intromission. The dual ACh-DA rhythms are generated locally by reciprocal regulation between ACh and DA signalling via nicotinic acetylcholine (nAChR) and dopamine D2 (D2R) receptors, respectively. Knockdown of choline acetyltransferase (ChAT) and D2R expression in the vsNAc diminishes intromission and ejaculation. We showed that ACh signalling promotes the initiation of intromission, whereas DA signalling sustains intromission by inhibiting the activities of D2R-expressing neurons in the vsNAc. Moreover, optogenetic activation of $ChAT^{vsNAc}$ neurons during intromission slows down the DA rhythm, a specific activity signature that precedes ejaculation, and leads to immediate ejaculation. Taken together, dual ACh-DA dynamics in the vsNAc coordinate sequential transitions of male copulatory behaviours from intromission to ejaculation.

Keywords: ventral shell of the nucleus accumbens (vsNAc), acetylcholine (ACh), dopamine (DA), dual ACh-DA rhythms, intromission, ejaculation

Introduction

In mammals, males engage in a stereotypical sequence of sexual behaviours when they encounter females in oestrous. This sequence of male sexual behaviours consists of courtship (appetitive) behaviours, such as sniffing and chasing, and followed by copulatory (consummatory) behaviours, such as mounting, intromission, and ejaculation in rodents[1–6]. Appropriate expression of sequential sexual behaviours is not only considered the attractivity of males, but also is important for the successful completion of sexual behaviours[7]. The neural mechanisms that regulate the sequential transitions of male sexual behaviours in the mammalian brain are largely unclear. For example, the nucleus accumbens (NAc) is thought to be involved in courtship behaviours, whereas the preoptic area (POA) has been implicated in copulatory behaviours[1,6]. However, recent studies indicated that POA primarily controls mounting[8–11]. Thus, the specific brain regions that regulate intromission and ejaculation are not yet identified, which hinders our understanding of the neural basis for controlling the intromission-to-ejaculation transition.

Accumulating studies have suggested that DA signalling functions as a primary driver for sexual motivation and behaviours[12–19]. Administration of cholinergic agonists in the preoptic area or substantia nigra changes the number or frequency of intromissions preceding ejaculation in rodents, implicating a regulatory role of ACh signalling during male copulatory behaviours[14,20,21]. It remains unclear, however, where and how precisely DA/ACh dynamics regulate male sexual behaviours[14–17,22–24]. Early microdialysis studies have detected an increase in extracellular DA concentration in the nucleus accumbens (NAc) during male sexual behaviours in rats[25–27]. Recent fibre photometry studies have recorded DA transients during intromission and ejaculation in male mice using the G protein-coupled receptor activation-based $(GRAB)_{DA}$ sensor with a high temporal resolution[15–17]. However, the regulatory mechanism and functional significance of DA dynamics in the NAc during male sexual behaviours remain unclear.

In this study, we hypothesise that ACh signalling modulates DA dynamics in the NAc to regulate male sexual behaviours, based on recent reports that ACh signalling regulates DA release from the dopaminergic axon terminals in the striatum[28–32]. By monitoring DA dynamics in various subregions of the NAc using the $GRAB_{DA2m}$ sensor[15,16], we found that real-time DA dynamics in the ventral shell of NAc (vsNAc) closely aligned with the sequential transitions of sexual behaviours in male mice. Consistent with our hypothesis, we observed a unique signature of dual ACh-DA rhythms in the vsNAc during intromission. Ex vivo brain slice imaging and computational modelling revealed that the dual ACh-DA rhythms were generated by reciprocal regulation between ACh and DA signalling via nAChR and D2R receptors, respectively. By optogenetic manipulations of ACh and DA release into the vsNAc, we demonstrated that dual ACh and DA dynamics in the vsNAc cooperatively drive the sequential transitions of male copulatory behaviours.

Results

DA dynamics in the vsNAc closely align with serial transitions of male sexual behaviours

After sniffing and chasing receptive female mice, male mice engage in repeated cycles of mounting and intromission, which culminate in an ejaculation followed by a brief falling and immobile phase (Fig. 1a). To study DA dynamics in the NAc during male sexual behaviours, we performed fibre photometry recording at the NAc of C57BL/6J male mice following injection in the NAc with adeno-associated virus (AAV) expressing $GRAB_{DA2m}$ sensor in neurons under human synapsin promotor (hSyn) (Fig. 1b). Since the NAc is anatomically heterogeneous[33–36], we examined DA dynamics in different subregions of the NAc by inserting optic fibres into the core (c), medial shell (ms), or ventral shell (vs) of the NAc, which was classified based on the expression pattern of substance P (Fig. 1c, d)[37]. Distinct patterns of extracellular DA dynamics were detected in the cNAc, msNAc, and vsNAc during male sexual behaviours (Fig. 1e-j). Both

vsNAc and cNAc, but not msNAc, exhibited an increase of $GRAB_{DA2m}$ signals that corresponded to all of the sequential transitions of male sexual behaviours, from the initial encounter of female mice to the final intromission-to-ejaculation transition (Fig. 1e-g; Supplementary Table 1). Among these, only the vsNAc exhibited a 1-2 Hz rhythmic fluctuation of $GRAB_{DA2m}$ signals during intromission, which appeared to be concurrent with the intromission thrust rhythm (Fig. 1h-j; Supplementary Table 2). These observations identify the vsNAc as a candidate brain region where DA dynamics may regulate the sequential transitions from intromission to ejaculation.

Local regulation of DA rhythm in the vsNAc during intromission

The ventral tegmental area (VTA) comprises a heterogeneous population of dopaminergic neurons (DA^{VTA} neurons) that, depending on their genetic and anatomical characteristics, send axonal projections to different target regions, such as in the NAc[33,35]. By two-colour cholera toxin B subunit (CTB)-mediated retrograde labelling, we found that the vsNAc and msNAc received projections from the anterolateral (al) VTA and the posteromedial (pm) VTA, respectively (Extended Data Fig. 1a-c).

To compare the activities of the dopaminergic neurons in the alVTA and pmVTA during male sexual behaviours, we unilaterally injected AAV-hSyn-DIO-GCaMP6s and inserted optical fibres into the alVTA or pmVTA of *DAT-ires-Cre* (DAT^{Cre}) mice, respectively (Extended Data Fig. 1d). Consistent with the different projection patterns, fibre photometry recording revealed that alVTA, but not pmVTA, neurons exhibited GCaMP (Ca^{2+}) dynamics in accordance with $GRAB_{DA2m}$ dynamics in the vsNAc during male sexual behaviours (Extended Data Fig. 1e-h; Supplementary Table 3). However, we did not observe rhythmic fluctuation of Ca^{2+} dynamics in the alVTA or pmVTA during intromission (Extended Data Fig. 1e).

We also performed fibre photometry to monitor the neuronal activity in DA^{VTA} axons projecting to the vsNAc ($DA^{VTA \rightarrow vsNAc}$) by injecting AAV-hSyn-DIO-GCaMP6s into the VTA and

inserting optical fibres into the vsNAc of *DAT*^{Cre} mice (Extended Data Fig. 1i). Unlike neuronal activity in the somata of alVTA, the Ca^{2+} dynamics in $DA^{VTA \rightarrow vsNAc}$ axons was similar to $GRAB_{DA2m}$ dynamics in the vsNAc, both in terms of high signal intensity and rhythmic fluctuations during intromission (Extended Data Fig. 1j, k; Supplementary Table 4). By recording the 405 nm isosbestic GCaMP control signals, we confirmed that the rhythmic GCaMP signals in the vsNAc reflected real neuronal activity rather than motion noises during intromission (Extended Data Fig. 1k). These observations suggest that DA dynamics in the vsNAc is regulated locally within the vsNAc and, to some extent, independent of the somata localised in the VTA.

Dual ACh-DA rhythms in the vsNAc during intromission

Previous studies have shown that ACh released from cholinergic interneurons promote DA release from DA^{VTA} axons in the striatum[28–32]. By immunohistochemistry of choline acetyltransferase (ChAT) in *DAT*^{Cre} mice, in which DA neurons were marked by GFP expression, we confirmed the existence of cholinergic interneurons ($ChAT^{vsNAc}$) in the proximity of the DA^{VTA} axons in the vsNAc (Extended Data Fig. 2a-c). To test our hypothesis that ACh signalling regulate DA dynamics in the vsNAc during male sexual behaviours, we unilaterally injected AAV-hSyn-DIO-GCaMP6s and inserted optic fibres into the vsNAc of *ChAT-ires-Cre* (*ChAT*^{Cre}) male mice (Extended Data Fig. 2d-f; Supplementary Table 5). Fibre photometry recording revealed that $ChAT^{vsNAc}$ neurons exhibited rhythmic activity during intromission (Extended Data Fig. 2f). Next, we examined the ACh dynamics in the vsNAc by injecting AAV-hSyn-$GRAB_{ACh3.0}$ into the vsNAc of C57BL/6J mice (Extended Data Fig. 2g-i; Supplementary Table 5). Similar to the rhythmic fluctuation of $GRAB_{DA2m}$ signals, we also observed the rhythmic fluctuation of $GRAB_{ACh3.0}$ signals during intromission (Extended Data Fig. 2i). These results are consistent with the idea that the rhythmic activity of cholinergic interneurons may regulate the rhythmic release of ACh and possibly DA in the vsNAc during intromission.

Next, we performed dual fibre photometry imaging to simultaneously monitor ACh and DA dynamics after AAV-mediated expression of green fluorescent $GRAB_{ACh3.0}$ and red fluorescent $GRAB_{rDA2m}$ in the vsNAc of C57BL/6J male mice (Fig. 2a). Importantly, we observed a specific signature of dual ACh and DA rhythms during intromission (Fig. 2b). By the wavelet coherence analysis, we found that the coherence between ACh and DA rhythms around 1-4 Hz band was significantly increased during intromission (Fig. 2c, d, Extended Data Fig. 2j; Supplementary Table 6, 7). Both ACh and DA rhythms were characterised by a frequency of 1.5–2.2 Hz by fast Fourier transform analysis (Fig. 2e). The ACh rhythm, but not DA rhythm, appeared just before the onset of intromission: the 1.5–2.2 Hz power of ACh rhythm was significantly higher than that of DA rhythm from 6-s before to 2-s after the intromission onset (Fig. 2f; Supplementary Table 6).

To assess the time-lag between ACh and DA rhythms during intromission, we compared the ACh/DA rhythm with the pelvic thrust rhythm by analysing the dynamic changes in the body size of male and female mice in the video (Fig. 2g). By plotting the ACh and DA rhythms around every thrusting event, we found the trough of ACh rhythm was ~0.1 s before, whereas that of DA rhythm was ~0.1–0.2 s after the thrusting (Fig. 2h). Moreover, the ACh rhythm, but not DA rhythm, persisted during the short pauses of pelvic thrusting during long intromissions (Fig. 2g). Taken together, these observations suggest that the ACh rhythm may function as the primary driver to generate the dual ACh-DA rhythm during intromission (Fig. 2e-h).

Signatures of the intromission preceding ejaculation (IPE)

While the majority of intromissions do not lead to ejaculation (intromission only (IO)), the last intromission typically transitioned into ejaculation (intromission preceding ejaculation (IPE)) during a successful cycle of sexual behaviours (Fig. 2i). Thus, a comparison of dual ACh-DA dynamics between IO and IPE may provide insights into the neural basis for controlling the intromission-to-ejaculation transition. Interestingly, the coherence of the dual ACh-DA rhythms

was significantly enhanced at the intromission onset of IPE relative to IO (Extended Data Fig. 2k, l; Supplementary Table 7). While the dual 1.5–2.2 Hz ACh-DA rhythms continued till the termination of IO (Fig. 2j), there was a specific slowdown of the 1.5–2.2 Hz DA rhythm just before ejaculation that coincides with the big surge of DA release in the IPE (Fig. 2k). Importantly, this brief suppression of DA rhythm was only observed in the vsNAc (Fig. 2l; Supplementary Table 6), not in the msNAc or cNAc, during the offset of IPE (Extended Data Fig. 2m; Supplementary Table 8), suggesting that it may be a prerequisite for the intromission-to-ejaculation transition.

ACh signalling regulates DA release in the vsNAc

To examine whether ACh signalling could regulate DA release from DA^{VTA} axons in the vsNAc, we injected AAV-hSyn-FLEX-ChrimsonR and AAV-hSyn-$GRAB_{DA2m}$ into the vsNAc of *ChAT*^{Cre} mice followed by ex vivo NAc brain slice imaging coupled with optogenetics and pharmacological treatments (Fig. 3a-c). Optogenetic activation of $ChAT^{vsNAc}$ neurons evoked an immediate and robust increase in $GRAB_{DA2m}$ signals in the NAc slices (Fig. 3b, c). This cholinergic stimulation of DA release was suppressed by nAChR antagonist DhβE at all frequencies (Fig. 3b, c). Similarly, the cholinergic activation of DA release was suppressed by mAChR antagonist atropine during 20 or 40 Hz stimulation of $ChAT^{vsNAc}$ neurons (Fig. 3b, c). In response to 1 or 10 Hz stimulation of $ChAT^{vsNAc}$ neurons, however, the blockade of mAChR induced a sharp increase of $GRAB_{DA2m}$ signals (Fig. 3b, c), possibly owing to the disinhibition of mAChR-mediated suppression of ACh release[38]. Accordingly, in situ hybridisation detected the expression of all five mAChR1-5 (*Chrm1-5*) in the majority of $ChAT^{vsNAc}$ neurons (Extended Data Fig. 3; Supplementary Table 9). In addition, DA^{VTA} neurons expressed both nAChR[39] and mAChR1-5 (Extended Data Fig. 3; Supplementary Table 9). These results suggest that ACh can promote DA release via nAChR signalling, but may also inhibit DA release in some contexts via mAChR signalling in the vsNAc.

DA signalling reciprocally regulates ACh release in the vsNAc

To examine whether DA signalling reciprocally regulated the activity of $ChAT^{vsNAc}$ neurons, we performed ex vivo Ca^{2+} imaging with NAc slices following injection of AAV-Syn-FLEX-ChrimsonR into the VTA and AAV-hSyn-DIO-GCaMP6s into the vsNAc of *ChAT*^{Cre};*DAT*^{Cre} mice (Fig. 3a, d, e). Optogenetic (1 Hz) stimulation of $DA^{VTA\rightarrow NAc}$ axons evoked different responses in the $ChAT^{NAc}$ neurons: ~20% increased, ~30% decreased, and ~50% exhibited no change of Ca^{2+} dynamics (Fig. 3e). By contrast, higher (≥10 Hz) frequency stimulation of $DA^{VTA\rightarrow NAc}$ axons increased the activity of ~40% $ChAT^{NAc}$ neurons and decreased the activity of ~30% $ChAT^{NAc}$ neurons (Fig. 3e). Notably, a small subset of $ChAT^{NAc}$ neurons displayed rhythmic fluctuation of Ca^{2+} dynamics in the NAc slices (Fig. 3d), which was consistent with the rhythmic fluctuation of Ca^{2+} dynamics in $ChAT^{vsNAc}$ neurons and rhythmic release of ACh in the vsNAc observed by in vivo fibre photometry during intromission (Extended Data Fig. 2d-i).

The observation of both *Drd1*$^{+}$$ChAT^{+}$ and *Drd2*$^{+}$$ChAT^{+}$ neurons in the vsNAc (Fig. 3f, g; Supplementary Table 10) raised two potential mechanisms for the regulation of $ChAT^{vsNAc}$ neurons by DA signalling: 1) inhibition of $ChAT^{vsNAc}$ neurons via D2R-mediated Gi/o signalling; 2) activation of $ChAT^{vsNAc}$ neurons via D1R-mediated Gs signalling[40]. To probe these possibilities, we injected AAV-Syn-FLEX-ChrimsonR and AAV-hSyn-$GRAB_{ACh3.0}$ into the vsNAc of *ChAT*^{Cre} mice (Fig. 3a, h-k). Optogenetic activation of $ChAT^{vsNAc}$ neurons increased $GRAB_{ACh3.0}$ signals in the NAc slices, which was suppressed by D2R agonist bromocriptine under all conditions except for 40 Hz stimulation (Fig. 3h, i). Thus, the D2R-mediated inhibition of $ChAT^{NAc}$ neurons could suppress the release of ACh from $ChAT^{NAc}$ neurons following ≤20 Hz optogenetic stimulation (Fig. 3i). Next, we investigated whether ACh release was also modulated by D1R signalling in the NAc slices by application of D1R agonist SKF38398. Activation of D1R signalling caused distinct changes in ACh release in the NAc slices, with 12.1% (up), 50.4% (down), and 37.5% (no change)

in $GRAB_{Ach3.0}$ signals (Fig. 3j, k). Taken together, these results suggest the reciprocal regulation of ACh release by DA signalling in the vsNAc, which is potentially mediated by D1R or D2R expressed on $ChAT^{vsNAc}$ neurons.

Modelling of dual Ach-DA rhythms by reciprocal regulation between ACh and DA signalling

To further study how the dual ACh-DA rhythms were generated by reciprocal regulation between ACh and DA in the vsNAc during intromission, we performed computational modelling using a simplified neuronal assemblage consisting of the dopaminergic ($DA_{sim}^{VTA\rightarrow vsNAc}$) axon terminals, cholinergic neurons ($ChAT_{sim}^{vsNAc}$), and the extracellular environment (Fig. 4a, Extended Data Fig. 4a-e). In this modelling, we defined the release probability measurement (RPM) of the neuronal assemblage as a measure of the intensity of neuronal activity (Fig. 4b). We set $Activation$ as a constant value to mimic the external stimuli, such as the spontaneous firing of each neuronal assemblage or stimulation by other neurons (Extended Data Fig. 4a, b). Additionally, the $Receptor$ function represents the effect of each receptor upon binding of ACh or DA (Fig. 4b). Both $Activation$ and $Receptor$ constantly change the RPM that determines the volume of neurotransmitter (NT) released to the extracellular environment (Fig. 4b).

The binding of DA to different dopamine receptors activates distinct intracellular G protein signalling to regulate neuronal activity: D1R triggers Gs signalling to activate neuronal activity, whereas D2R activates G protein-gates inwardly rectifying potassium (GIRK) channels-mediated signalling to inhibit neuronal activity[40–42]. On the other hand, the binding of ACh to nAChR causes a rapid influx of cations, such as Na^+ and Ca^{2+}, to activate neuronal activity[43,44]. Herein, we focused on nAChR rather than mAChR1-5 to simplify our modelling to explore the characteristics of D1R and D2R relative to nAChR. We hypothesised that the characteristics of each receptor consist of two axes: the effect intensity (effect: RE) with which the receptor changes neuronal activity; the

processing speed (speed: RS) of the receptor in affecting the neuronal activity upon binding of ACh or DA (Fig. 4b).

Cholinergic activation is required for modelling dual ACh-DA rhythms

The goal of the modelling is to estimate the RE and RS values of each receptor to minimize the $Diff(NT_{sim}, NT_{real})$, i.e., the difference between simulated signals (NT_{sim}) and experimentally recorded in vivo GRAB signals (NT_{real}). To simplify the model, both the RS and RE values of the nAChR were defined as 1, and the RS and RE values of D1R and D2R relative to the nAChR were explored (Fig. 4a, b). Based on the ex vivo imaging (Fig. 3) and in situ hybridisation results (Extended Data Fig. 3) and previous report of D2R expression in dopaminergic neurons[45], we placed D1R and D2R on $ChAT_{sim}^{vsNAc}$ neurons and nAChR and D2R on $DA_{sim}^{VTA\rightarrow vsNAc}$ axon terminals in this model (Fig. 4a). Importantly, we found that the simulated dual rhythms of ACh and DA closely resembled the experimentally recorded ACh and DA rhythms (Fig. 4c).

To investigate the relative contribution of $ChAT_{sim}^{vsNAc}$ neurons and $DA_{sim}^{VTA\rightarrow vsNAc}$ axon terminals, we compared the similarity between NT_{real} and NT_{sim} ($Diff(NT_{sim}, NT_{real})$) in three activation patterns: $ChAT_{sim}^{vsNAc}$ and $DA_{sim}^{VTA\rightarrow vsNAc}$ ($Activation_{(1,1)}$); only $ChAT_{sim}^{vsNAc}$ ($Activation_{(1,0)}$); only $DA_{sim}^{VTA\rightarrow vsNAc}$ ($Activation_{(0,1)}$) (Extended Data Fig.4a, b). The similarity between NT_{real} and NT_{sim} rhythms suggested that the $Activation_{(1,1)}$ and $Activation_{(1,0)}$ conditions were much better than the $Activation_{(0,1)}$ condition to simulate dual ACh-DA rhythms (Fig. 4d; Supplementary Table 11). These observations suggest that the activation of cholinergic neurons is necessary to generate dual ACh-DA rhythms.

D2R, but not D1R, is required for modelling dual ACh-DA rhythms

We visualised the explored values of the RS and RE for each assumed receptor during the simulation. Notably, the RS of D2R was in the range of 5–50 ms, whereas the RS of D1R was approximately 350–400 ms (Fig. 4e), indicating that the processing speed of D2R is approximately 7–80 fold faster than that of D1R in our model. This finding is consistent with the fact that the GIRK-mediated D2R signalling is much faster than Gs-mediated D1R signalling. On the other hand, the *RE* of D1R or D2R on $ChAT_{sim}^{vsNAc}$ neurons are approximately 1/100 or 1/50 of the *RE* of nAChR on $DA_{sim}^{VTA\rightarrow vsNAc}$ axon terminals, respectively. By contrast, the *RE* of D2R on $DA_{sim}^{VTA\rightarrow vsNAc}$ axon terminals is about 2 to 4 times of the *RE* of nAChR (Fig. 4f), such that the effect intensity of D2R on $DA_{sim}^{VTA\rightarrow vsNAc}$ axon terminals is hundreds fold larger than that of D2R on $ChAT_{sim}^{vsNAc}$ neurons in our model.

To determine the receptors essential for generating the dual ACh-DA rhythms, we performed simulations to evaluate the similarity between NT_{sim} and NT_{real} following ablation of each receptor (Fig. 4g, Extended Data Fig. 4f, g). Consistent with estimation that D2R has larger *RE* than D1R, the ablation of D2R, but not D1R, on $ChAT_{sim}^{vsNAc}$ neurons worsens the similarity between NT_{sim} and NT_{real} as compared with the full receptor condition (Fig. 4g; Supplementary Table 12). Similarly, the ablation of D2R or nAChR on $DA_{sim}^{VTA\rightarrow vsNAc}$ axon terminals significantly worsened the similarity between NT_{sim} and NT_{real}. These observations underscore the importance of D2R-mediated DA signalling and nAChR-mediated ACh signalling in the generation of dual ACh-DA rhythms.

Knockdown of ChAT and D2R in the vsNAc diminishes intromission and ejaculation

To validate our simulation results in vivo, we performed RNAi-mediated knockdown of ChAT, D1R, or D2R expression by injecting the vsNAc of male mice with AAV expressing short hairpin (sh)RNA targeting *Chat*, *Drd1* or *Drd2* mRNA (Fig. 4h). In situ hybridisation verified

efficacy of knockdown of target gene expression in the vsNAc (Fig. 4i-k, Extended Data Fig. 5a; Supplementary Table 13). After 3 weeks post AAV-shRNA injection, the sexual behaviour tests were conducted over a period of 3 weeks (Fig. 4h, Extended Data Fig. 5b-h). Consistent with the simulation results of in silico receptor ablation (Fig. 4g), knockdown of ChAT or D2R, but not D1R, expression in the vsNAc diminished the frequency of sexual behaviours, such as intromission and ejaculation, relative to the scrambled shRNA-expressing mice (Fig. 4l, m; Supplementary Table 14). Moreover, knockdown of ChAT or D2R prolonged the average latency of mounting, intromission, and ejaculation, whereas knockdown of D2R reduced the average number of bouts and total duration of mounting and intromission (Extended Data Fig. 5; Supplementary Table 15). Importantly, neither ChAT nor D2R knockdown affected the motor coordination of the mice as measured by the rotarod test (Fig. 4n; Supplementary Table 16), excluding the possibility that male sexual behaviours were affected indirectly by impairing motor coordination. These results indicate that both ACh and DA signalling play important roles during male copulatory behaviours. Based on the results of ex vivo brain slice imaging, computational modelling, and RNAi knockdown experiments, we concluded that the dual ACh-DA rhythms are likely generated in the vsNAc by reciprocal ACh-DA regulations mediated by nAChR and D2R signalling in $DA^{VTA\rightarrow vsNAc}$ axon terminals and D2R signalling in $ChAT^{vsNAc}$ neurons, respectively.

High level of DA signalling in the vsNAc is important for the maintenance of intromission

A high level of extracellular DA was observed in the vsNAc, and only the vsNAc exhibited the 1.5–2.2 Hz DA rhythm during intromission (Fig. 1). To examine whether DA signalling plays a crucial role during intromission, we optogenetically manipulated the $DA^{VTA\rightarrow vsNAc}$ axon terminals to investigate whether changing DA dynamics in the vsNAc could affect male copulatory behaviours. Specifically, we bilaterally injected AAV-Ef1a-DIO-ChR2 or AAV-Ef1a-DIO-eNpHR3.0 into the VTA and inserted optic fibres into the vsNAc of DAT^{Cre} mice (Fig. 5a). Notably,

optogenetic activation of the $DA^{VTA \rightarrow vsNAc}$ axons either before intromission (during sniffing, chasing, or mounting) or during intromission (after two pelvic thrust movements) increased the total duration of intromission (Fig. 5b-e, Extended Data Fig. 6; Supplementary Table 17, 18). Additionally, optogenetic activation before intromission also increased the number of intromission bouts, although it did not immediately trigger intromission (Fig. 5b, Extended Data Fig. 6b). Conversely, optogenetic suppression of the $DA^{VTA \rightarrow vsNAc}$ axon terminals before or during intromission did not affect male sexual behaviours, possibly owing to incomplete suppression of DA signalling (see discussion). These results suggest that high level of DA signalling in the vsNAc promotes the initiation and maintenance of intromission.

DA-mediated inhibition of $D2R^{vsNAc}$ neurons sustains male sexual behaviours, whereas suppression of $D1R^{vsNAc}$ neurons ensures forward progression of sexual behaviours

To elucidate how DA dynamics regulate activity of D1R- and D2R-expressing neurons in the vsNAc during male sexual behaviours, we unilaterally injected AAV-hSyn-DIO-GCaMP6s and inserted optic fibres in the vsNAc of *Drd1-ires-Cre* (*$Drd1^{Cre}$*) and *Drd2-ire-Cre* (*$Drd2^{Cre}$*) mice, respectively (Fig. 5f-i, Extended Data Fig. 7a, b; Supplementary Table 19, 20). Fibre photometry recording revealed that the activity of both $D1R^{vsNAc}$ and $D2R^{vsNAc}$ neurons were suppressed during intromission (Extended Data Fig. 7a, b), despite the opposite effects of D1R (excitatory) and D2R (inhibitory) signalling on neuronal activity[40–42]. The simplest explanation for this paradoxical observation is that DA signalling preferentially activates the D2R-mediated inhibition of neuronal activities during intromission owing to the different thresholds for D1R and D2R activation[46,47,12] (see discussion).

To study the functional importance of suppression of $D1R^{vsNAc}$ and $D2R^{vsNAc}$ neurons during intromission, we specifically expressed ChR2 in the $D1R^{vsNAc}$ or $D2R^{vsNAc}$ neurons by injecting AAV-Ef1a-DIO-ChR2 into the vsNAc of *$Drd1^{Cre}$* and *$Drd2^{Cre}$* mice, respectively (Fig. 5j-

p, Extended Data Fig. 7c-f; Supplementary Table 21, 22). While optogenetic activation of D1R^{vsNAc} neurons before intromission did not affect male sexual behaviours, optogenetic stimulation of these neurons during intromission increased the total mounting duration by inducing repetitive mounting behaviours (Fig. 5k-p, Extended Data Fig. 7c, d). Thus, the suppression of D1R^{vsNAc} neurons during intromission is critical for ensuring the forward progression of male sexual behaviours.

On the other hand, optogenetic activation of D2R^{vsNAc} neurons during sniffing, chasing, mounting, and intromission immediately stopped any of these sexual behaviours (Fig. 5k, l). Consequently, opto-stimulation of D2R^{vsNAc} neurons before intromission increased total mounting duration and prolonged ejaculation latency (Fig. 5m, n), whereas opto-stimulation of D2R^{vsNAc} neurons during intromission decreased total intromission duration (Fig. 5o, Extended Data Fig. 7e, f). These observations indicate that DA-mediated suppression of D2R^{vsNAc} neurons is necessary for sustaining male sexual behaviours including intromission (Fig. 5q).

ACh signalling in the vsNAc promotes sequential transitions of intromission and ejaculation

To study how ACh signalling in the vsNAc regulated male sexual behaviours, we bilaterally injected AAV-Ef1a-DIO-ChR2 or AAV-Ef1a-DIO-eNpHR3.0 and inserted optic fibres into the vsNAc of *ChAT*^{Cre} male mice (Fig. 6a). Next, we optogenetically activated or inhibited the ChR2- or eNpHR3.0-expressing ChAT^{vsNAc} neurons, respectively, before or during intromission and examined the effects on male copulatory behaviours (Fig. 6b-g, Extended Data Fig 8). While optogenetic activation of ChAT^{vsNAc} neurons before intromission did not affect mating behaviours, optogenetic inhibition of ChAT^{vsNAc} neurons before intromission significantly prolonged the latency of mounting, intromission, and ejaculation (Fig. 6b, d, e, Extended Data Fig 8a; Supplementary Table 23). These results suggest that ACh signalling in the vsNAc is required for the initiation of mounting and intromission.

Notably, optogenetic activation of ChAT^{vsNAc} neurons during intromission induced rapid ejaculation by shortening the ejaculation latency and increasing the ejaculation likelihood (Fig. 6c, f, g; Supplementary Table 24). Moreover, the number of mounting or intromission bouts and the mounting total duration were also decreased (Extended Data Fig 8g-i). In contrast, optogenetic inhibition of ChAT^{vsNAc} neurons during intromission did not affect mating behaviours (Fig. 6f, g, Extended Data Fig 8g-k; Supplementary Table 24). These results indicate that activation of ACh signalling in the vsNAc triggers the intromission-to-ejaculation transition.

To study how activation of ACh signalling changed DA dynamics during intromission, we injected AAV-hSyn-GRAB$_{DA2m}$ and AAV-Syn-FLEX-ChrimsonR into the vsNAc of *ChAT^{Cre}* mice and monitored DA dynamics by fibre photometry during optogenetic stimulation of ChAT^{vsNAc} neurons (Fig. 6h-j). Interestingly, optogenetic activation of ChAT^{vsNAc} neurons during intromission resulted in a decrease of the 1.5–2.2 Hz power of the DA rhythm followed by a brief suppression of DA release, which resembled the characteristic slowdown of DA rhythm just before ejaculation during IPE (Fig. 6k, l; Supplementary Table 25). Taken together, these results suggest that activation of ACh signalling in the vsNAc during intromission leads to a slowdown of DA rhythm followed by immediate ejaculation (Fig. 6m).

Discussion

Dual ACh-DA dynamics in the vsNAc drive sequential transitions of male copulatory behaviours

The neural mechanisms that regulate the sequential transitions of male copulatory behaviours, such as mounting, intromission, and ejaculation, remain unclear. Previous studies have identified specific brain regions that control mounting[8–11], but the brain regions that regulate intromission and ejaculation are to be elucidated. Here, we identified the vsNAc as a critical brain region where dual ACh-DA dynamics aligned with and coordinate the sequential transitions from intromission to ejaculation. In particular, the vsNAc exhibits a unique signature of 1.5–2.2Hz dual

ACh-DA rhythms that are concurrent with the pelvic thrust rhythm during intromission. The ACh rhythm, but not DA rhythm, appears before the intromission onset and persists during the short pauses of pelvic thrusting during intromission. These observations suggest that ACh rhythm functions as the primary driver for generating the dual ACh-DA rhythms during intromission. We proposed that dual ACh-DA rhythms play a crucial role in the maintenance of intromission possibly by reinforcing the pelvic thrust rhythm. By optogenetic manipulations of ACh and DA release in the vsNAc, we showed that ACh signalling promoted the initiation of intromission, whereas DA signalling was important for sustaining intromission through the suppression of $D2R^{vsNAc}$ neurons. Furthermore, optogenetic activation of $ChAT^{vsNAc}$ neurons during intromission elicits immediate ejaculation by triggering a slowdown of DA rhythm–a specific activity signature that typically precedes ejaculation during IPE. Taken together, these results demonstrate that dual ACh-DA dynamics harmonise in the vsNAc to drive the sequential transitions of male copulatory behaviours from intromission to ejaculation.

Dual ACh-DA rhythms are generated by reciprocal regulations between ACh and DA release

Both $ChAT^{vsNAc}$ neurons and $DA^{VTA\rightarrow vsNAc}$ axons, but not DA^{VTA} somata, exhibited rhythmic neuronal activity during intromission, suggesting that the dual ACh-DA rhythms are regulated locally by mutual interaction between $ChAT^{vsNAc}$ neurons and $DA^{VTA\rightarrow vsNAc}$ axons. Consistent with this idea, we showed reciprocal regulation between ACh and DA release mediated by nAChR and D1R or D2R signalling in the NAc brain slices by ex vivo (GRAB or GCaMP) imaging with optogenetic and pharmacological manipulations. Computational modelling suggests that the dual ACh-DA rhythms in the vsNAc are generated by reciprocal ACh-DA regulations via D2R signalling in cholinergic neurons and D2R and nAChR signalling in dopaminergic axon terminals. Accordingly, the shRNA-mediated knockdown of ChAT and D2R, but not D1R, expression in the vsNAc diminished the probability of sexual behaviours, such as intromission and

ejaculation. Although we primarily focused on nAChR, D1R, and D2R to simplify our modelling of the dual ACh-DA rhythms, we could not exclude a potential role for mAChRs in the generation of dual ACh-DA rhythms during intromission. A recent study also reported the dual ACh-DA (~2 Hz) rhythms in the dorsal striatum during reward delivery, but these rhythms were not generated by direct interaction between ACh and DA release within the striatum[28]. Thus, it is possible that the dual ACh-DA rhythms can be generated by different mechanisms to regulate diverse biological processes.

Distinct functions of D1R and D2R signalling during male sexual behaviours

Our finding that $D1R^{vsNAc}$ and $D2R^{vsNAc}$ neurons, which are largely distinct neuron populations, were both suppressed during intromission is consistent with the proposed "threshold" hypothesis for D1R and D2R-mediated DA signalling during sexual behaviours[12,47]. Since D2R has a higher affinity than that of D1R[46], DA signalling may preferentially cause the D2R-mediated suppression of $D2R^{vsNAc}$ neurons, while $D1R^{vsNAc}$ neurons are not activated during intromission (Supplementary Table 26). Alternatively, it is plausible that suppression of $D2R^{vsNAc}$ neurons may indirectly lead to active suppression of $D1R^{vsNAc}$ neurons through unknown mechanisms. Importantly, optogenetic activation of $D2R^{vsNAc}$ neurons either before or during intromission rapidly stopped the sexual behaviours. It is plausible that activation of $D2R^{vsNAc}$ neurons is associated with aversive emotions[48,49], which may function as an "off" switch to pause male sexual behaviours. Thus, the DA-mediated suppression of $D2R^{vsNAc}$ neurons is necessary for sustaining male sexual behaviours such as intromission.

The highest level of DA release was observed at the onset of female encounter or during ejaculation, which might cause the activation of $D1R^{vsNAc}$ neurons to regulate the initiation and termination of male sexual behaviours. Optogenetic activation of $D1R^{vsNAc}$ neurons during intromission increased the total mounting duration by inducing repetitive mounting behaviour. It is

plausible that optogenetic stimulation of $D1R^{vsNAc}$ neurons mimics the activation of $D1R^{vsNAc}$ neurons at female encounter and, thus, resetting the sexual behaviours. Therefore, the suppression of $D1R^{vsNAc}$ neurons during intromission ensures the forward progression of male sexual behaviours by preventing animals from returning to the previous behavioural sequences, such as mounting.

ACh signalling regulates ejaculation timing by triggering slowdown of DA rhythm

We observed a specific slowdown of DA rhythm just before ejaculation that coincides with a big surge of DA release during IPE. Accordingly, optogenetic activation of $ChAT^{vsNAc}$ neurons resulted in a similar slowdown of DA rhythm followed by immediate ejaculation. This optogenetics-induced suppression of DA rhythm was even stronger than the suppression of DA rhythm just before ejaculation during IPE (Fig. 6l). By contrast, optogenetic inhibition of $DA^{VTA\rightarrow vsNAc}$ axons during intromission did not elicit ejaculation (Supplementary Table 27). In the striatum, cholinergic interneurons make monosynaptic or polysynaptic axo-axonic contact on DA^{VTA} axons[30,38]. ACh released from cholinergic interneurons can evoke action potentials at the DA^{VTA} axons and promote DA release from proximal and distant DA axons via the action potential propagation[29,31]. Therefore, optogenetic activation of $ChAT^{vsNAc}$ neurons may have a larger effect on DA dynamics in the vsNAc than direct optogenetic manipulation of $DA^{VTA\rightarrow vsNAc}$ axons. Moreover, optogenetic stimulation of $ChAT^{vsNAc}$ neurons results in a high level of ACh signalling, which then leads to a brief suppression of DA signalling, both of which may be required for inducing ejaculation.

It should be noted that pharmacological inhibition of mAChRs enhanced the release of DA following 1 or 10 Hz opto-stimulation of $ChAT^{vsNAc}$ neurons in the NAc brain slices, suggesting that mAChRs could suppress DA release in specific contexts of ACh signalling. Optogenetic stimulation of $ChAT^{vsNAc}$ neurons may cause a surge of ACh signalling, leading to the suppression

of DA release by activating the inhibitory mAChRs on DA^{VTA} axons. Similarly, we observed that the coherence of ACh-DA rhythms between 1–4 Hz frequency was significantly higher at the onset of IPE than IO. This increased coherence of dual ACh-DA rhythms probably results in a higher level of ACh signalling, which in turn may cause the suppression of DA rhythm by activating the inhibitory mAChRs. Future studies are warranted to elucidate the detailed mechanism for why dual ACh-DA rhythms specifically results in the slowdown of DA rhythm and triggers the intromission-to-ejaculation transition during IPE, but not during IO.

To the best of our knowledge, this study is the first report of ejaculation induction by manipulating a small population of genetically defined neurons in freely behaving animals. Our results reveal, for the first time, a crucial role of ACh signalling in regulating the timing of ejaculation in mammals. Premature ejaculation (PE) is a prevalent sexual disorder affecting approximately 20–30% of sexually active men[50]**.** Moreover, PE has been observed in relatively high percentages in Parkinson's disease patients, which is thought to be the result of the medications and the disease itself, with DA signalling being the common contributing factor[51]**.** Selective serotonin reuptake inhibitors are also used to treat patients with PE[52]**.** Although the exact mechanism is not yet fully understood, serotonin can affect the activity of dopamine neurons and DA release[53]**.** Therefore, these drugs may affect DA dynamics and, in turn, regulate ejaculation latency. We anticipate that our findings will be a starting point for more sophisticated studies into the molecular and neural mechanisms that govern ejaculation timing and the potential development of new therapeutics for sexual dysfunctions in humans.

Methods

Mice

All animal experiments were performed at the International Institute for Integrative Sleep Medicine, University of Tsukuba, in accordance with the guidelines for animal experimentation. The experiments were approved by the animal experiment committee of each institute and were conducted in accordance with NIH guidelines. Mice were given food and water *ad libitum* and maintained at a temperature of 23 °C and relative humidity of 50%, with a 12-h light/12-h dark cycle. C57BL/6J mice (ID# 000664 from Charles River), male *ChAT*^{Cre} mice (B6;129S6-Chattm2(cre)Lowl/J; ID# 006410, Jaxson Laboratory)[54], male *DAT*^{Cre} mice (B6.SJLSlc6a3tm1.1(cre)Bkmn/J; ID# 006660, Jaxson Laboratory)[55], male *Drd1*^{Cre} mice (B6.FVB(Cg)-Tg(Drd1-cre)EY262Gsat/Mmucd; ID# 030989-UCD from MMRRC originally from GENSAT BAC Tg project), and male *Drd2*^{Cre} mice (B6.FVB(Cg)-Tg(Drd2-cre)ER44Gsat/Mmucd; ID# 032108-UCD from MMRRC originally from GENSAT BAC Tg project) were used in this study. The ages of the mice used for the experiments were 8 to 32 weeks.

Viruses

The plasmids of AAV-hSyn-DIO-GCaMP6s (serotype 9), AAV-Syn-FLEX-rc[ChrimsonR-tdTomato] (serotype 1), AAV-hSyn-DIO-EGFP (serotype 9), AAV-EF1a-double floxed-hChR2(H134R)-EYFP-WPRE-HGHpA (serotype 9), AAV-Ef1a-DIO-EYFP (serotype 9), and AAV-Ef1a-DIO eNpHR3.0-EYFP (serotype 9) were purchased from Addgene. The plasmids of AAV[shRNA]-CMV>mCherry-U6>Scramble_shRNA (serotype 9), AAV[shRNA]-mCherry-U6>mChat[shRNA#1] (serotype 9), and AAV[shRNA]-mCherry-U6>*Drd1*[shRNA#1] (serotype 9) were purchased from vector-builder. AAV-H1-shScramble-4-CMV-mCHERRY (serotype 10) and AAV-H1-shD2R-4-CMV-mCHERRY (serotype 10) were shared by the University of Tsukuba. The plasmids of AAV-hSyn-GRAB_DA2m ($GRAB_{DA2m}$) (serotype 9), AAV-hSyn-GRAB_ACh3.0

($GRAB_{ACh3.0}$) (serotype 9), and AAV-hSyn-rDA2m ($GRAB_{rDA2m}$) (serotype 9) were provided by Yulong Li. All AAVs were prepared at the University of Tsukuba. AAV titres were 9.79×10^{11} – 6.24×10^{14} genomic copies/mL.

Stereotaxic surgery

AAVs were produced using the triple-transfection helper-free method and purified as previously described[56]. The titres of AAVs were determined by qPCR and purified viruses were stored in aliquots at -80°C. Details of AAVs are listed in Supplementary Table 28. Adult male mice (aged > 8 weeks) were stereotactically injected with AAVs and implanted with optical fibres after at least one week post AAV injection. The animals were anaesthetised with isoflurane (2–4%) and placed in a stereotaxic frame (David Kopf Instruments, Tujunga, CA). Viruses were stereotaxically delivered to the brains of mice at 2–5 months of age as described previously[57]. In brief, virus was delivered unilaterally (0.2 μL of AAV-hSyn-$GRAB_{DA2m}$, AAV-hSyn-DIO-GCaMP6s, AAV-hSyn-$GRAB_{ACh3}$, and AAV-hSyn-$GRAB_{rDA2m}$) or bilaterally (0.3 μL of AAV-Syn-FLEX-rc[ChrimsonR-tdTomato], AAV-hSyn-DIO-EGFP, AAV-EF1a-double floxed-hChR2(H134R)-EYFP-WPRE-HGHpA, AAV-Ef1a-DIO EYFP, AAV-Ef1a-DIO eNpHR3.0-EYFP. Immediately after surgery, mice were placed on a heated pad individually and then returned to their home cage following recovery from anaesthesia. Animals were allowed at least 2 weeks of recovery in a reversed light/dark room following surgery prior to being tested in behavioural assays.

For retrograde tracing, we then injected 0.3 μL of the retrograde tracer cholera toxin subunit B (CTB) conjugated with AlexaFluor-594 and AlexaFluor-488 (Thermo Fisher Scientific) into the msNAc and vsNAc. Mice were perfused 5 days after CTB injection. Whole brain sections were prepared.

Immunohistochemistry

For histological analysis, animals were perfused with 4% paraformaldehyde, and the brains were dissected and post-fixed overnight in 4% paraformaldehyde. Brains were sectioned at 60 μm thickness using a vibrating microtome (Leica) and immunostaining was performed as described previously[58]. In brief, sections were collected in PBS and were treated with permeabilisation solution (1% Triton in PBS) at room temperature for 3 h, followed by incubation with the blocking buffer (10% Blocking One [Nacalai Tesque] with 1% Triton X-100 in PBS), and incubated overnight at 4 °C using primary antibodies in the blocking buffer. After washing with PBS three times, brain slices were incubated with secondary (second) antibody in blocking buffer at 4 °C overnight. The slices were stained with NeuroTrace fluorescent Nissl stain (Invitrogen, N-21279) or 4', 6-diamidino-2-phenylinodole (DAPI) (Dojindo, D523), washed, mounted, and coverslipped.

Primary antisera used were chicken anti-GFP (Novus Biologicals; 1:4,000), rat anti-GFP (Nacalai Tesque; 1:2,000), rat anti-Substance P (Merck & Co., Inc.; 1:500), rabbit anti-Substance P (ImmunoStar Inc.; 1:1500), goat anti-mCherry (Sicgen; 1:2,000), rat anti-mCherry (Thermo Fisher Scientific; 1:500), goat anti-ChAT (Merck & Co., Inc.; 1:500), mouse anti-TH (Santa Cruz Biotechnology; 1:250), sheep anti-Digoxigenin-POD (Roche Applied Science; 1:2,000), and sheep anti-Fluorescein-POD (Roche Applied Science; 1:2,000).

Secondary antisera used were as follows: Alexa Fluor 488 donkey anti-rat (Jackson ImmunoResearch; 1:500), Alexa Fluor 488 donkey anti-rabbit (Jackson ImmunoResearch; 1:500), Alexa Fluor 488 donkey anti-chicken (Jackson ImmunoResearch; 1:500), Alexa Fluor 647 donkey anti-rat (Jackson ImmunoResearch; 1:500), Alexa Fluor 647 donkey anti-rabbit (Jackson ImmunoResearch; 1:500), Alexa Fluor 647 donkey anti-goat (Jackson ImmunoResearch; 1:500), Alexa Fluor 647 donkey anti-goat (Thermo Fisher Scientific; 1:1,000), Cy3 donkey anti-rat (Jackson ImmunoResearch; 1:500), Cy3 donkey anti-rabbit (Jackson ImmunoResearch; 1:500),

Cy3 donkey anti-goat (Jackson ImmunoResearch; 1:500), and Cy3 donkey anti-guinea pig (Jackson ImmunoResearch; 1:500).

In situ hybridisation

The cDNA fragments of mouse *Drd1*, *Drd2*, *Chrm1*, *Chrm2*, *Chrm3*, *Chrm4*, and *Chrm5* were amplified by PCR using antisense primers containing the T7 promoter sequence. In vitro transcription was performed with PCR-amplified templates using T7 RNA polymerase (Hoffman La Roche AG, Basel, Switzerland) to synthesise antisense RNA probes (Supplementary Table 29). Two-color in situ hybridisation was performed as previously described[59]. Briefly, the mice were deeply anaesthetised with isoflurane and transcardially perfused with ice-cold 10% sucrose in Milli-Q water, followed by ice-cold 4% PFA. The collected brain samples were post-fixed with 4% PFA at 4 °C overnight, followed by displacement with 30% sucrose in PBS containing 0.1% diethylpyrocarbonate at 4 °C overnight. Coronal brain sections (40 μm) were prepared using a cryostat (Leica Biosystems, Nussloch, Germany). Brain sections were treated with proteinase K (Roche), acetylated, and then incubated with hybridisation buffer containing antisense RNA probes at 60 °C for 16 h. After stringent washing, the brain sections were incubated with peroxidase (POD)-conjugated anti-FITC antibody (Roche Applied Science, Germany; 1:2,000) or POD-conjugated anti-Digoxigenin antibody (Roche Applied Science, Germany; 1:500) at 4 °C overnight. To sequentially use a POD-conjugated antibody, a 2% sodium azide solution was used to inactivate HRP. TSA systems (TSA-FITC and TSA-Biotin) and NeutrAvidin Protein, DyLight™ 550 (Thermo Fisher Scientific; 1:500) conjugate (Thermo Fisher Scientific) were used to visualise mRNA signals.

Analysis of the brain slice images

Imaging of brain sections was conducted using a LSM800, NanoZoomer XR (Hamamatsu Photonics, Hamamatsu City, Japan) and Axio Zoom V16 on-axis zoom microscope (Carl Zeiss AG, Oberkochen, Germany). To confirm the AAV-infected sites in the fibre photometry (Fig. 1, 2, 5, 6, Extended Data Fig.1, 2, 7), RNAi silencing (Fig. 4i-k, Extended Data Fig. 5), and optogenetics experiments (Fig. 5, 6 and Extended Data Fig. 6-8), coronal brain sections were immunostained for substance P (SP)[37]. The recording site was identified based on fibre tracking of the brain histological section sample. Each subregion of the NAc was defined as follows. While the cNAc shows a low level of SP expression, the msNAc and vsNAc are characterised by high levels of SP expression. Moreover, the msNAc is located on the medial side of the cNAc, and the vsNAc is sandwiched between the cNAc and the dense SP axons (ventral pallidum) (Fig. 1c).

Quantification of mAChR1-5, Drd1, *and* Drd2 *on* $ChAT^{vsNAc}$ *and* DA^{VTA} *neurons in the brain slice images*

To confirm the expression patterns of ChAT and dopamine receptors (*Drd1* and *Drd2*) in the NAc (Fig. 3g), ChAT and *mAChR1-5* (*mAChR1*, *mAChR2*, *mAChR3*, *mAChR4*, *mAChR5*) in the vsNAc (Extended Data Fig. 3c), and TH and *mAChR1-5* in the VTA (Extended Data Fig. 3d), we manually annotated the target marker$^+$ somata using a multi-point function and extracted the NAc subregions by polygon selection in ImageJ/Fiji. The number of signals in each subregion was counted using schemes implemented in Python 3.7.2. Expression ratios were calculated based on the number of regions of each target marker. The *Drd1* or *Drd2* ratio in the $ChAT^{vsNAc}$ neurons was calculated as the target marker (*Drd1* or *Drd2*)$^+$$ChAT^+$ / $ChAT^+$ (%) (Fig. 3g). To calculate the *mAChR1-5* ratio in the $ChAT^{vsNAc}$ neurons, the target marker (*mAChR1-5*)$^+$$ChAT^+$ / $ChAT^+$ (%) was calculated (Extended Data Fig. 3c). To calculate the *mAChR1-5* ratio in DA^{VTA} neurons, the

target marker (*mAChR1-5*)$^{+}$TH^{+} / TH^{+} (%) was calculated (Extended Data Fig. 3d). The mean values for each mouse are shown (Fig. 3g, Extended Data Fig. 3c, d).

The shRNA-mediated knockdown in the vsNAc

AAV[shRNA]-CMV>mCherry-U6>Scramble_shRNA, AAV[shRNA]-mCherry-U6>mChat[shRNA#1], AAV[shRNA]-mCherry-U6>*Drd1*[shRNA#1], AAV-H1-shScramble-4-CMV-mCHERRY, AAV-H1-shD2R-4-CMV-mCHERRY) at 100 nL/min with a Hamilton syringe using a micropump. To calculate the knockdown ratio of target marker by shRNA, we prepared three types of images in which shRNA (mCherry), the target marker (GFP: *Drd1*, *Drd2*, or ChAT), and DAPI were observed around the vsNAc. The target^{+} (mCheery^{+}, GFP^{+}, or DAPI^{+}) somata were extracted from each image using OpenCV 4.5.5. First, cv2.medialBlur with a kernel size of 9 was applied to the image to reduce noise. Next, the histogram of the image was calculated using cv2.calcHist, and the peak of the histogram was obtained using scipy.signal.find_peaks with a distance of 5. V_{pk} was set to the pixel value corresponding to the maximum peak. The image was binarized with a threshold of V_{pk} minus 10, and the contours of the target^{+} somata were extracted by applying cv2.findContours to the binarized image. The mode and method were set to becv2.RETR_EXTERNAL and cv2.CHAIN_APPROX_SIMPLE, respectively. We selected the contours of DAPI and the target markers with areas between 10 and 200 in the images. The knockdown ratios were calculated from the region numbers of the target markers, shRNA, and DAPI. The shRNA knockdown ratio was calculated as the target marker (*Drd1*, *Drd2* or ChAT)$^{+}$shRNA^{+} / DAPI^{+}shRNA^{+} (%). The mean values for each mouse are shown in Fig. 4i-k.

Sexual behaviour test

Hormone priming

Stimulus females in oestrus were induced as described previously[8]. C57BL/6J female mice were ovariectomised at > 8 weeks of age. One week after the surgery, estradiol benzoate dissolved in sesame oil (10 μg/0.1 mL; EB) was administered to all female mice as a stimulus. More than 1 d after the first EB injection, all female mice were hormonally primed with subcutaneous injections of EB 48 and 24 h before testing, and they received progesterone dissolved in sesame oil (500 μg/0.1 mL) 4–6 h before testing to ensure high sexual receptivity. Male mice were exposed to all female mice in their home cages. Female mice were examined for ejaculation using a copulatory plug. Female stimuli that experienced ejaculation one time were used in the sexual behaviour test. Male mice were exposed to a different receptive female mouse from that used in the previous test.

Behavioural analysis

Sexual behaviours, including mounting, intromission, ejaculation, and falling, were analysed based on videos obtained using cameras. The video frames were manually annotated with these sexual behaviours using BORIS[60]. The duration and number of mountings, intromissions, and ejaculations were recorded for each mouse. The latency of each behaviour was calculated by subtracting the female onset from the onset of each behaviour. For optogenetic manipulation before intromission, appetitive behaviours, including sniffing and chasing a female mouse, were manually annotated (Fig. 5b, k, 6b).

Visualisation of the intromission thrust movements

The body regions of two male and female mice during intromission were extracted using Python 3.7.2 and OpenCV 4.5.5. to visualise their thrusting movements. First, video frames with intromission behaviours were extracted from the original videos, and the intromission frames were then converted into grayscale images. Next, the contrast-limited adaptive histogram equalisation (CLAHE) operator was applied to the grayscale images to improve their contrast (clipLimit = 2.0,

tileGridSize = (3, 3)). The histogram of each CLAHE image was calculated using cv2.calcHist. The histogram had several pixel values with a height of 500 pixels. With V_{500} representing the minimum pixel value, the binarization operator was applied to the CLAHE image using threshold V_{500}. Conversely, the createBackgroundSubstractorMOG2 (BSMOG2) was applied to the grayscale images, and the median smoothing filter with a kernel size of 25 was applied to the BSMOG2 images. The binarized CLAHE images were multiplied by the smoothed BSMOG2 images, and black (zero) pixels were extracted from the multiplied images as mouse body regions (Fig. 2g). The Z-scored lines of mouse body region sizes and the bottom point as thrusting behaviour were plotted using MATLAB (Fig. 2h).

Fibre photometry experiment

i) Fibre photometry recording

For fibre photometry imaging of neurotransmitters, AAV-hSyn-$GRAB_{DA2m}$, AAV-hSyn-$GRAB_{ACh3.0}$, or AAV-hSyn-$GRAB_{rDA2m}$ was injected unilaterally into the NAc of C57BL/6J mice. For fibre photometry imaging of Ca^{2+} dynamics, AAV-hSyn-DIO-GCaMP6s was injected unilaterally into the VTA of *DAT*^{Cre} mice or the vsNAc of *ChAT*^{Cre} mice, *Drd1*^{Cre} mice, or *Drd2*^{Cre} mice. More than 1 week after virus injection, a 200-μm core, 0.50 NA optical fibre (Thorlabs and Lymyth) was implanted unilaterally into the vsNAc or VTA. The mice were allowed to recover for at least 2 weeks before the experiments.

To monitor animal behaviour during fibre photometry imaging, (method 1) a web camera (Logicool HD Webcam C525r, Logitech International S.A., Switzerland) was used. To synchronise the fibre photometry recording and the video recording that captures mouse behaviours, (method 2) a USB camera (FLIR USB3.0 Vision Camera # CM3-U3-13Y3M-CS; Teledyne FLIR, Wilsonville, OR) was used. The USB camera released the shutter at a rate of 10 fps based on the Fibre Photometry Console signals. On the day of the experiment, mice were recorded in their home cages

with regular chow feeding for 2 h in the dark phase. More than 10 min after the onset of recording, an oestrous female mouse was introduced into the home cages of male mice. The recording was stopped more than 2 h after introducing the female. After the test, we reviewed the video footage and examined the female mouse's vagina to identify any signs of ejaculation by the male mouse.

For DA, ACh, or GCaMP imaging, the fluorescence emitted by $GRAB_{DA2m}$, $GRAB_{ACh3.0}$, or GCaMP was collected under a blue LED (CLED465), and the fluorescence emitted by $GRAB_{rDA2m}$ was collected under a green LED (CLED560). The $GRAB_{DA2m}$, $GRAB_{ACh3.0}$, and GCaMP signals were recorded at an acquisition rate of > 10 Hz, and those of $GRAB_{ACh3.0}$ and $GRAB_{rDA2m}$ were recorded at an acquisition rate of 20 Hz using Doric Neuroscience Studio (version 5. 4. 1. 5, Doric Lenses Inc.). The LED output intensity was adjusted so that the light excitation of the optical fibre cable was approximately 30 $\mu W/mm^2$. The signals of $GRAB_{DA2m}$, $GRAB_{ACh3.0}$, and GCaMP between 500–540 nm and those of $GRAB_{rDA2m}$ between 580–680 nm were recorded.

ii) Data analysis for fibre photometry signals

All fibre photometry signals, except for the two-colour imaging of GCaMP6s, $GRAB_{ACh3.0}$, and $GRAB_{rDA2m}$, were transformed into 10 Hz by a MATLAB interp1 function to align with the behavioural events. As peri-event time plots (PETP), To analyse the signal dynamics around the onset and offset of each sexual behaviour, we extracted the signal intensities for 20 s before and after the behavioural events (for a total of 40 s). The $\Delta F/F$ ratio was calculated by dividing the signal intensity in each frame by the mean value for 20 s before the behavioural events. The $\Delta F/F$ ratio was z-scored against the extracted 40-s signal intensities. To compare the intensity changes of each signal, mean $\Delta F/F$ every 10 s in each behavioural event, in which the baseline was the mean for the first 10 s were plotted (Fig. 1e-g, Extended Data Fig. 1g, h, j, 2e, h, 7a, b).

To analyse the DA rhythm (Fig. 1h-j, 2l, Extended Data Fig. 2m) or dual ACh-DA rhythms (Fig. 2e, j, k) during intromission, we calculated the power spectrum using MATLAB FFT with a 3 s window allowing a 0.3 s overlap or 0.25 s overlap, respectively. To show that ACh rhythm, but

not DA rhythm, started before intromission, we analysed the sum of the power spectrum of the 1.5–2.2 Hz band of ACh/DA rhythms every 2 s observed from 10 s before to 10 s after the intromission onset (Fig. 2f). To analyse the DA rhythm during intromission, we collected the sum of the power spectrum every 0.2 Hz band during intromission behaviour (Fig. 2l, Extended Data Fig. 2m).

To analyse the coherence between $GRAB_{ACh3.0}$ and $GRAB_{rDA2m}$, first we prepared the extracted signals around intromission. The $GRAB_{ACh3.0}$ and $GRAB_{rDA2m}$ signals were extracted 20 s before the intromission onset to 10 s before the intromission onset and 10 s before the intromission offset to 10 s after the intromission offset. These two signals were combined, and 50 s length signals were prepared. Using these 50 s length signals, MATLAB wavelet coherence was applied. Average values of the wavelet coherence over all the target events were calculated and it was visualised by heatmap plot (Fig. 2c). To compare the coherence between $GRAB_{ACh3.0}$ and $GRAB_{rDA2m}$ around the intromission, we calculated the mean of the wavelet coherence around <1 Hz, 1–4 Hz, and >4 Hz every 10 s (Fig. 2d, Extended Data Fig. 2j) and the mean of the wavelet coherence in IO and IPE around 1-4 Hz every 5 s (Extended Data Fig. 2k, l).

To visualise ACh and DA dynamics in the vsNAc during each thrust in the intromission phase, we extracted the time point that showed the bottom of the area of the mouse body, which was assumed to be the pelvic thrusting behaviour. Based on the bottom time point, we extracted $GRAB_{ACh3.0}$ and $GRAB_{rDA2m}$ around the thrusting behaviour ± 0.5 s (Fig. 2g, h).

To analyse the $GRAB_{DA2m}$ dynamics with optogenetic activation of $ChAT^{vsNAc}$ neurons using ChrimsonR, we calculated the power spectrum using MATLAB FFT with a 3 s window allowing 0.3 s overlap and collected the power spectrum of the 1.5–2.2 Hz band observed from 10 s before the ejaculation onset to the ejaculation onset during intromission (Fig. 6l).

Ex vivo imaging and optogenetics

We used 8–21-week-old *ChAT*^{Cre} or *ChAT*^{Cre}; *DAT*^{Cre} male mice for imaging and optogenetic experiments during acute brain histological section preparation. These mice were injected with the following AAV vectors into the target brain areas at least 3 weeks prior to the experiments: (i) for imaging the DA response to photostimulation of cholinergic neurons in the vsNAc, AAV-Syn-FLEX-ChrimsonR-tdTomato and AAV-hSyn-GRAB$_{DA2m}$ were injected into the vsNAc of *ChAT*^{Cre} mice (Fig. 3b, c); (ii) for imaging Ca^{2+} in cholinergic neurons in response to photostimulation of dopaminergic axons from the VTA, AAV-Syn-FLEX-ChrimsonR-tdTomato and AAV-hSyn-DIO-GCaMP6s were injected into the VTA and vsNAc of *ChAT*^{Cre};*DAT*^{Cre} double transgenic mice, respectively (Fig. 3d, e); (iii) for imaging the ACh response to photostimulation of cholinergic neurons in the vsNAc, AAV-Syn-FLEX-ChrimsonR-tdTomato and AAV-hSyn-GRAB$_{ACh3.0}$ were injected into the vsNAc of *ChAT*^{Cre} mice (Fig. 3h-k). Acute brain histological sections were prepared using a slightly modified N-methyl-d-glucamine (NMDG) protective recovery method[61,62]. Briefly, mice were anaesthetised with isoflurane and then cardiovascularly perfused with ice-cold NMDG-artificial cerebrospinal fluid (aCSF) consisting of 93 mM NMDG, 93 mM HCl, 2.5 mM KCl, 1.2 mM NaH_2PO_4, 30 mM $NaHCO_3$, 20 mM HEPES, 25 mM D-glucose, 5 mM Na-ascorbate, 2 mM thiourea, 3 mM Na-pyruvate, 10 mM $MgSO_4$, and 0.5 mM $CaCl_2$ (pH 7.4, adjusted with HCl, oxygenated with 95% O_2/5% CO_2). The brains were sliced to a thickness of 200 μm in ice-cold NMDG-aCSF using a vibratome (Leica VT1200S). Slices containing the striatum were incubated in NMDG-aCSF at 32 °C for 12 min and then in HEPES-aCSF consisting of 124 mM NaCl, 2.5 mM KCl, 1.2 mM NaH_2PO_4, 24 mM $NaHCO_3$, 5 mM HEPES, 12.5 mM D-glucose, 2 mM $CaCl_2$, and 1 mM $MgSO_4$ (~310 mOsm, oxygenated with 95% O_2/5% CO_2) at room temperature for at least 1 h. Slices were transferred into a chamber under an upright fluorescence microscope (Zeiss AxioExaminer D1, HXP120, 20x or 40x water-immersion objective lens) and submerged in perfused HEPES-sCSF at 32–35 °C. Fluorescence signals were acquired using an

EM-CCD camera (Andor iXon Ultra 888, 1024 × 1024 pixels, 16 bit) and iQ software (Andor), in which green and red fluorescence were observed using a Zeiss filter set 38HE (excitation 470/40 nm, emission 525/50 nm) and Zeiss filter set 43 (excitation 545/25 nm, emission 605/70 nm), respectively. Green fluorescence included $GRAB_{DA2m}$, $GRAB_{ACh3.0}$, and GCaMP6s. The frame rate was 5 fps, except for experiments with Ca^{2+} imaging or bath application of SKF38398 (frame rate of 0.2 fps). For optical stimulation, an optical fibre was placed just above the target area and outside the field of view, and optical stimuli (579 nm, 10-ms pulses for 30 s, Shanghai Laser) were controlled using a function generator (Master-9, AMPI). A data acquisition system (Digidata® 1440A Low-noise data acquisition system, Molecular Devices) was employed to synchronise the timing of optical stimuli and image acquisition. This system allowed for precise monitoring of the timing of both processes.

Image analysis was performed using Fiji and R. All images were subtracted from the background signal, which was the mean fluorescence intensity outside the field of view of the objective. Bleaching was corrected by linear interpolation of the medians of fluorescence intensity for 5–10 s before and after photostimulation. For optogenetics and imaging with $GRAB_{DA2m}$ or $GRAB_{ACh3.0}$, the edges of the 1024 × 1024-pixel images were removed to obtain 1008 × 1008-pixel images because the edges were outside the field of view of the objective lens. A total of 196 (16 × 16) square ROIs with 63 pixels per side were created in a 1008 × 1008 image, and the mean fluorescence intensity within each ROI was calculated. ROIs without $GRAB_{DA2m}$ or $GRAB_{Ach3.0}$ expression (mean intensity <100) were excluded from the analysis. The mean fluorescence intensity was z-scored against the value obtained for 20 s before photostimulation. For experiments with SKF38398, bleaching was corrected using the median values for 60 s before and 120–180 s after bath application, and the fluorescence intensity was z-scored against the values for 60 s before the application. For Ca^{2+} imaging with GCaMP6s, ROIs were set on the somata of the neurons expressing GCaMP6s.

ROIs were classified using the Mann–Whitney U test, with values for 5 s before and 10 s after photostimulation for the GCaMP experiments (Fig. 3e), and 60 s before and 120 s after the application of SKF38398 for the $GRAB_{ACh3.0}$ experiments (Fig. 3k).

Computational modelling of DA and ACh dynamics

As we observed similar dynamics in GRAB and GCaMP ($GRAB_{DA2m}$ and GCaMP6s of dopaminergic axons in the vsNAc [Fig 1 and Extended Data Fig. 1i-k], $GRAB_{ACh3.0}$ and GCaMP6s of cholinergic neurons in the vsNAc [Extended Data Fig. 2d-i]) by fibre photometry imaging, we hypothesised that (1) the neuronal activity of the neuronal ensemble reflects the amount of NT (neurotransmitter) released; (2) the GCaMP dynamics reflect the release probability of the NT. Based on these hypotheses, we developed a computational model to estimate the cellular environment in which neurons and receptors are involved in generating dual ACh-DA rhythms during intromission. In this model, we set neuronal assembly ($ChAT_{sim}^{vsNAc}$ and $DA_{sim}^{VTA\rightarrow vsNAc}$), the internal activity of neurons (release probability measurement, RPM), NT release (ACh_{sim} and DA_{sim}) based on the RPM, receptors expressed on neurons (D1R, D2R, and nAChR), and the extracellular environment in which the NT can be released. To mimic the change of the amount of the extracellular NT over time, in this model, we assumed the three steps of cycle: (i) the activation of target neurons by the external stimuli; (ii) NT released from the target neurons; (iii) the effect of the receptor by binding NT to the receptor on the target neurons. These cycles were repeated a certain number of times and, during this period, we recorded the RPM and amount of NT_{sim} released from the neurons which was determined based on the RPM value. Through this model, we attempted to estimate the appropriate cellular environment, including the type of receptors or neurons involved, by minimising $Diff(NT_{sim}, NT_{real})$, the difference between the actual ACh-DA dynamics in vivo (NT recorded by fibre photometry: NT_{real}) and model-simulated ACh-DA dynamics (NT generated by the model: NT_{sim}) (Fig. 4a, b, Extended Data Fig. 4).

Hypothetical neurons and receptors used in this simulation were identified based on ex vivo imaging (Fig. 3), the in situ hybridisation results (Extended Data Fig. 3), and previous reports[45]. As neurons and receptors, we placed D1R and D2R in $ChAT_{sim}^{vsNAc}$ neurons, as well as D2R and nAChR in $DA_{sim}^{VTA \rightarrow vsNAc}$ axon terminals. From our ex vivo imaging, we found that inhibitory mAChR may function as an autoreceptor (Fig. 3b, c). However, since all subtypes of *mAChR* were expressed on $ChAT^{vsNAc}$ and DA^{VTA} neurons (Extended Data Fig. 3), to simplify our modelling, we focused on D1R, D2R, and nAChR receptors in this experiment (Fig. 4a).

(i) Activation of target neurons by the external stimuli

To mimic the cellular environment that neurons are activated by the external stimuli, in this modelling, we assumed that the RPM which reflects the intensity of neuronal activity was changed by the external stimuli or the effect of the receptor expressed on the neurons. $Activation$ includes the spontaneous activity of the target neurons and stimulation of neurons by substances other than ACh and DA. Here, we defined that the $Activation$ continuously adds a certain value to the target neuron. Thus, the value added as an external stimulus to the RPM of the target neurons every cycle was constant.

(ii) Release of NT from the target neurons

To mimic the manner of NT release, we defined that the volume of NT_{sim} released to the extracellular environment from the neurons was determined by the RPM value of the neurons. In this model, the volume of NT_{sim} released is equivalent to the RPM value if RPM is positive and 0 if RPM is negative (Fig. 4b). Additionally, we defined the diffusion function of DA to mimic the in vivo extracellular DA diffusion mechanism[63]. The time course and intensity of the DA diffusion were investigated using this model (Extended Data Fig. 4c-e).

(iii) Effect of the receptor by binding NT to the receptor on the target neurons

Next, we considered the strategy to mimic the behaviour of nAChR, D1R, and D2R. As reported in previous studies, DA receptors are GPCRs that are thought to respond more slowly than nAChR, the ionotropic receptor[40–44]. Incorporating these insights, we defined the characteristics of each receptor using two variables: RE (receptor efficacy), the effect intensity which changes RPM; RS (receptor speed), the latency where the $Receptor$ function affects RPM from the time that NT_{sim} binds to the receptor. In this experiment, to simplify the setting, we set the nAChR related variables as constant values (nAChR's RE=1, and the RS=1), and estimated the characteristics of D1R and D2R by exploring their RE and RS. RE of D1R and D2R was searched over a range of positive values, and their RS was searched over a range of natural numbers.

For example, when ACh_{sim} binds to the nAChR expressed on the $DA_{sim}^{VTA \rightarrow vsNAc}$ axon terminals, there is an increase in the RPM of the $DA_{sim}^{VTA \rightarrow vsNAc}$ axon terminal ACh_{sim} × 1 (nAChR's RE=1) one step later (nAChR's RS=1). Since the D1R receptor is an excitatory GPCR, we defined its operation as follows: when D1R receives DA_{sim}, "D1R's RS" step later, the RPM is increased to DA_{sim} × "D1R's RE." By contrast, we defined operation of the D2R receptor, an inhibitory GPCR, receiving DA_{sim} as "D2R's RS" step later, RPM is decreased by a factor of DA_{sim} × "D2R's RE". With these receptors' settings, we conducted computational modelling to estimate the RE and RS values.

To estimate receptor efficacy (RE) and receptor speed (RS) of DA receptors, we explored RE and RS values which minimise $Diff(NT_{sim}, NT_{real})$, the difference between NT_{sim} and NT_{real} using Bayesian optimisation (Fig. 4b). We used Optuna[64], an automatic hyperparameter optimisation software framework, to determine the best values for RE and RS using $Diff(NT_{sim}, NT_{real})$ as an indicator. We used the following values as a fixed value throughout exploration. The value added by $Activation$ is 1. The number of trials conducted to estimate RE and RS of D1R and D2R was approximately 1,000 to 10,000, depending on the experimental design. In each experimental design, out of these trials, the one representing the smallest

$Diff(NT_{sim}, NT_{real})$, the condition where NT_{sim} and NT_{real} are most similar, was used to define RE and RS of D1R and D2R. To express the effect speed of each receptor in seconds, the RS of each receptor and DA diffusion step were divided by 200, the sampling rate (Fig. 4e, Extended Data Fig. 4e).

Experiment 1: Performance comparison by the different activation patterns

To prove which neurons should be activated in the generation of dual ACh-DA rhythms, we compared the $Diff(NT_{sim}, NT_{real})$ under the following three conditions: (1) $ChAT_{sim}^{vsNAc}$: on / $DA_{sim}^{VTA \to vsNAc}$: on (= $Activation_{(1,1)}$); (2) $ChAT_{sim}^{vsNAc}$: on / $DA_{sim}^{VTA \to vsNAc}$: off (= $Activation_{(1,0)}$); (3) $ChAT_{sim}^{vsNAc}$: off / $DA_{sim}^{VTA \to vsNAc}$: on (= $Activation_{(0,1)}$) (Fig. 4d, Extended Data Fig. 4a, b).

Experiment 2: Estimation of RE and RS of dopamine receptors

To reveal the RE and RS values of D1R and D2R generating dual ACh-DA rhythms, we estimated the RE and RS values under the $Activation_{(1,1)}$ with full receptors condition (D1R and D2R on $ChAT_{sim}^{vsNAc}$, and D2R and nAChR on $DA_{sim}^{VTA \to vsNAc}$). We focused on trials showing the converged $Diff(NT_{sim}, NT_{real})$ because otherwise the trial indicated the failure of the variable search (Fig. 4e, f).

Experiment 3: Performance comparison by deletion of each candidate receptor

To find which candidate receptor is important for the generation of dual ACh-DA rhythms, we estimated the RE and RS values under five conditions which delete a target receptor; deletion of (1) D1R on $ChAT_{sim}^{vsNAc}$, (2) D2R on $ChAT_{sim}^{vsNAc}$, (3) D2R on $DA_{sim}^{VTA \to vsNAc}$, (4) D2R on both $ChAT_{sim}^{vsNAc}$ and $DA_{sim}^{VTA \to vsNAc}$, and (5) nAChR on $DA_{sim}^{VTA \to vsNAc}$. Then, we compared the $Diff(NT_{sim}, NT_{real})$ among these five conditions and the condition with full receptor using the estimated each candidate RE and RS of D1R and D2R (Fig. 4g, Extended Data Fig. 4f, g).

Gene knockdown experiments

Sexual behaviour test with shRNA treatment

To silence the gene expression of ChAT, D1R, or D2R, AAV-CMV-mCherry-U6-shmChAT, AAV-CMV-mCherry-U6-shD1R, or AAV-H1-shD2R-CMV-mCherry was injected into the vsNAc of C57BL/6J male mice. In the control group, AAV-H1-shScramble-CMV-mCherry or AAV-CMV-mCherry-U6-shScramble was injected into the vsNAc of C57BL/6J male mice. Three weeks (± 1 day) following AAV injection, male mice underwent the sexual behaviour test once a week (± 1 day) for 3 weeks. Male mice were relocated to the test room 30 min before starting the test. After the acclimation period, a female stimulus mouse was introduced into the home cage of a male mouse. Video recordings were conducted over the next 2 h. After the test, we reviewed the video footage and inspected the female mice to determine whether male mice exhibited sexual behaviours. The intromission and ejaculation rates were then calculated based on the frequency of these behaviours observed across the three tests (Fig. 4h, l, m). The average latency, the number of bouts, and total duration of each behaviour were calculated across the tests (Extended Data Fig. 5).

Rotarod test with shRNA treatment

A rotarod test was conducted to confirm the motor coordination of mice expressing shRNA in the vsNAc. To silence the gene expression of ChAT, D1R, or D2R, AAV-CMV-mCherry-U6-shmChAT, AAV-CMV-mCherry-U6-shD1R, or AAV-H1-shD2R-CMV-mCherry was injected into the vsNAc of C57BL/6J male mice. For the control group, AAV-H1-shScramble-CMV-mCherry or AAV-CMV-mCherry-U6-shScramble was injected into the vsNAc of C57BL/6J male mice. More than 3 weeks after the AAV injection, male mice were moved to the test room. After more than 15 min, we initiated a habituation process for the rotarod machine. During this phase, mice were placed in the stationary state of the rotarod machine for 2 min. After acclimatisation, the male mice

were allowed to practice on a rotarod for 2 min (12 rpm). Subsequently, we conducted three rotarod tests (each gradually increasing from 5 to 40 rpm for 300 s). We recorded the latency period before the mice were dropped from the rotarod machine. Between each test, the mice were allowed a 5-min break. The median value was plotted as an effect of motor coordination (Fig. 4n).

Optogenetics experiments

To activate $DA^{VTA\rightarrow vsNAc}$ axons, $ChAT^{vsNAc}$ neurons, $D1R^{vsNAc}$ or $D2R^{vsNAc}$, AAV-Ef1a-DIO-ChR2-EYFP, or AAV-hSyn-DIO-EGFP was injected bilaterally into the VTA of *DAT*^{Cre} mice or the vsNAc of *ChAT*^{Cre} mice, *Drd1*^{Cre} mice, or *Drd2*^{Cre} mice. To inhibit $DA^{VTA\rightarrow vsNAc}$ axon terminals or $ChAT^{vsNAc}$ neurons, AAV-Ef1a-DIO-eNpHR3.0-EYFP or AAV-Ef1a-DIO-EGFP was injected bilaterally into the VTA of *DAT*^{Cre} mice or the vsNAc of *ChAT*^{Cre} mice. After more than 2 weeks, 200-μm core and 0.50 NA optical fibres (Thorlabs and Lymyth) were bilaterally implanted into the vsNAc. The mice were allowed to recover for at least 2 weeks before conducting the experiments. Before the tests, it was confirmed that the male mice ejaculated twice. This was determined by verifying the presence of a plug in the vagina of the female mouse.

Two tests were performed: manipulation before (20 Hz, 10 ms) and during intromission (20 Hz, 10 ms) (Fig. 5b-e, k-p, 6b-g, Extended Data Fig. 6, 7c-f, 8). The interval between each test was at least 4 days. On the test day, the mice were moved to the experimental room 1 h before the experiments in the dark phase and optical fibres were connected to their heads. The axonal terminals of dopaminergic and cholinergic neurons in the vsNAc were activated (462 nm, Shanghai Laser) or inhibited (579 nm, Shanghai Laser). We created a system using an electrical board to record the stimulation timing and manage the stimulation frequency using the Arduino UNO and Doric Neuroscience Studio. Video recordings and recordings of the optogenetic stimulation schedule were initiated simultaneously using Doric Neuroscience Studio. In each test, the experimenter observed the behaviour of the mice and turned on the switch to shine the laser. The

switch was immediately turned off if the target behaviour was prevented. If the male mice did not exhibit any sexual behaviour within 10 min of starting the test, the test was terminated and repeated on a different day. If the subject male mice did not ejaculate within 10 min after the onset of stimulation, we stopped the stimulation and confirmed the timing of ejaculation until 20 min after the onset of stimulation (Fig. 6b).

For manipulation before the intromission (20 Hz, 10 ms) test, the experimenter turned on the laser while observing sniffing, chasing, and mounting. When mounting was not prevented, the mice showed intromission, the stimulation was stopped, and the timing of ejaculation was confirmed. In the other case, the target behaviour was prevented within 10 min of starting the stimulation; accordingly, we stopped the stimulation and confirmed the timing of ejaculation. If the male mice did not ejaculate within 20 min of starting the stimulation, the test was terminated, and the ejaculation latency was recorded as 1,200 s.

For manipulation during the intromission tests (20 Hz, 10 ms), the experimenter turned on the laser when seeing the intromission, specifically when thrusting occurred more than twice. In cases where ejaculation was not observed within 10 min of starting the stimulation, the stimulation ceased, and we confirmed the timing of ejaculation within 20 min of starting the stimulation. The recorded ejaculation latency in such cases was 1,200 s.

Fibre photometry with optogenetics

To monitor DA dynamics when stimulating cholinergic neurons, AAV-Syn-FLEX-ChrimsonR-tdTomato and AAV-hSyn-$GRAB_{DA2m}$ were injected into the vsNAc of *ChAT*^{Cre} mice. Subsequently, optical fibres with a 200-μm core and 0.50 NA (Thorlabs and Lymyth) were bilaterally implanted in the vsNAc (Fig. 6h, i). The mice were allowed to recover for at least 2 weeks before performing the experiments. $GRAB_{DA2m}$ recordings were conducted without optogenetics to confirm the $GRAB_{DA2m}$ signals. After confirmation, bilateral optogenetic

manipulations without fibre photometry recordings were conducted to confirm optogenetic effects on behaviour. Target neurons were activated using a laser (579 nm, Shanghai Laser).

After confirming the behavioural expression, DA dynamics were recorded during optogenetic activation of cholinergic neurons in the vsNAc. In this experiment, unilaterally DA dynamics were monitored, and target neurons were activated during intromission. We created a system using an electrical board to record the stimulation timing and manage the stimulation frequency with the help of the Arduino UNO and Doric Neuroscience Studio. Fibre photometry recordings, video recordings using a USB camera (FLIR USB3.0 Vision Camera # CM3-U3-13Y3M-CS), and recordings of the optogenetic stimulation schedule were synchronised using Doric Neuroscience Studio. In each test, the experimenter observed the behaviour of the mice. When observing intromission, particularly more than two intromission-thrusting movements, the experimenter turned on the switch button to shine the laser. The fluorescence emitted by $GRAB_{DA2m}$ was recorded under a blue LED (CLED465) using a Doric fibre photometry system for DA imaging. $GRAB_{DA2m}$ was recorded at 10 Hz using Doric Neuroscience Studio (version 5.4.1.5). The LED output intensity was adjusted such that the amount of light exiting the optical fibre cable was approximately 30 $\mu W/mm^2$. The $GRAB_{DA2m}$ signals within the 500–540 nm range were recorded (Fig. 6j).

Quantification and statistical analysis

Recorded videos and histological samples were analysed blind to relevant variables, including administrated solution, genotype, prior housing condition, surgical procedure, and virus injection. Videos were manually annotated using BORIS. In particular, anogenital investigation (sniffing and chasing), mounting, repeated pelvic thrust (intromission), and ejaculation were scored for male sexual behaviours. After annotations, various parameters including latency, number, and duration were calculated for further analysis.

Data were processed and analysed using MATLAB, R, Python 3.7.2, and GraphPad PRISM 9.4.1 (GraphPad Software, San Diego, CA). All results are expressed as mean ± SEM. Data of non-paired samples were analysed with two-tailed non-parametric Mann–Whitney U test or Kruskal–Wallis test. All multiple comparisons were corrected with Dunn's multiple comparisons correction. Data of paired samples were analysed with two-way ANOVA followed by Šídák's post-hoc multiple comparison test. The significance threshold was held at $\alpha=0.05$, two-tailed (not significant [ns], $p > 0.05$; $*p < 0.05$; $**p < 0.01$; $***p < 0.001$; $****p < 0.0001$). Details are available in Supplemental Supplementary Table 1-25.

Data and code availability

Further information and requests for resources should be directed to and will be fulfilled by the Lead Contact, Qinghua Liu (liuqinghua@nibs.ac.cn). This study did not generate new unique reagents. The code and software used in this study will be freely available through GitHub or Zenodo once the paper is published.

References

1. Everitt, B. J. Sexual motivation: A neural and behavioural analysis of the mechanisms underlying appetitive and copulatory responses of male rats. *Neurosci. Biobehav. Rev.* **14**, 217–232 (1990).
2. Ågmo, A. Male rat sexual behavior. *Brain Res. Protoc.* **1**, 203–209 (1997).
3. Pfaus, J. G., Kippin, T. E. & Centeno, S. Conditioning and Sexual Behavior: A Review. *Horm. Behav.* **40**, 291–321 (2001).
4. Paredes, R. G. & Ågmo, A. Has dopamine a physiological role in the control of sexual behavior?: A critical review of the evidence. *Prog. Neurobiol.* **73**, 179–225 (2004).
5. Hull, E. M. & Dominguez, J. M. Sexual behavior in male rodents. *Horm. Behav.* **52**, 45–55 (2007).
6. Balthazart, J. & Ball, G. F. Topography in the preoptic region: Differential regulation of appetitive and consummatory male sexual behaviors. *Front. Neuroendocrinol.* **28**, 161–178 (2007).
7. Beach, F. A. Sexual attractivity, proceptivity, and receptivity in female mammals. *Horm. Behav.* **7**, 105–138 (1976).
8. Sano, K., Tsuda, M. C., Musatov, S., Sakamoto, T. & Ogawa, S. Differential effects of site-specific knockdown of estrogen receptor α in the medial amygdala, medial pre-optic area, and ventromedial nucleus of the hypothalamus on sexual and aggressive behavior of male mice. *Eur. J. Neurosci.* **37**, 1308–1319 (2013).
9. Wei, Y.-C. *et al.* Medial preoptic area in mice is capable of mediating sexually dimorphic behaviors regardless of gender. *Nat. Commun.* **9**, 279 (2018).
10. Karigo, T. *et al.* Distinct hypothalamic control of same- and opposite-sex mounting behaviour in mice. *Nature* **589**, 258–263 (2021).

11. Bayless, D. W. *et al.* A neural circuit for male sexual behavior and reward. *Cell* **186**, 3862-3881.e28 (2023).
12. Hull, E. M. *et al.* Opposite influence of medial preoptic D1 and D2 receptors on genital reflexes: Implications for copulation. *Life Sci.* **51**, 1705–1713 (1992).
13. Hull, E. M., Eaton, R. C., Moses, J. & Lorrain, D. Copulation increases dopamine activity in the medial preoptic area of male rats. *Life Sci.* **52**, 935–940 (1993).
14. Bitran, D. & Hull, E. M. Pharmacological analysis of male rat sexual behavior. *Neurosci. Biobehav. Rev.* **11**, 365–389 (1987).
15. Sun, F. *et al.* A Genetically Encoded Fluorescent Sensor Enables Rapid and Specific Detection of Dopamine in Flies, Fish, and Mice. *Cell* **174**, 481-496.e19 (2018).
16. Sun, F. *et al.* Next-generation GRAB sensors for monitoring dopaminergic activity in vivo. *Nat. Methods* **17**, 1156–1166 (2020).
17. Dai, B. *et al.* Responses and functions of dopamine in nucleus accumbens core during social behaviors. *Cell Rep.* **40**, 111246 (2022).
18. Fiorino, D. F. & Phillips, A. G. Facilitation of sexual behavior and enhanced dopamine efflux in the nucleus accumbens of male rats after D-amphetamine-induced behavioral sensitization. *J. Neurosci. Off. J. Soc. Neurosci.* **19**, 456–463 (1999).
19. Holstege, G. *et al.* Brain Activation during Human Male Ejaculation. *J. Neurosci.* **23**, 9185–9193 (2003).
20. Hull, E. M. *et al.* Brain localization of cholinergic influence on male sex behavior in rats: Agonists. *Pharmacol. Biochem. Behav.* **31**, 169–174 (1988).
21. Winn, P. Cholinergic stimulation of substantia nigra: effects on feeding, drinking and sexual behaviour in the male rat. *Psychopharmacology (Berl.)* **104**, 208–214 (1991).
22. Qian, T. *et al.* A genetically encoded sensor measures temporal oxytocin release from different neuronal compartments. *Nat. Biotechnol.* **41**, 944–957 (2023).

23. Hull, E. M., Muschamp, J. W. & Sato, S. Dopamine and serotonin: influences on male sexual behavior. *Physiol. Behav.* **83**, 291–307 (2004).

24. Hillegaart, V. & Ahlenius, S. Facilitation and inhibition of male rat ejaculatory behaviour by the respective 5-HT1A and 5-HT1B receptor agonists 8-OH-DPAT and anpirtoline, as evidenced by use of the corresponding new and selective receptor antagonists NAD-299 and NAS-181. *Br. J. Pharmacol.* **125**, 1733–1743 (1998).

25. Pleim, E. T., Matochik, J. A., Barfield, R. J. & Auerbach, S. B. Correlation of dopamine release in the nucleus accumbens with masculine sexual behavior in rats. *Brain Res.* **524**, 160–163 (1990).

26. Pfaus, J. G. *et al.* Sexual behavior enhances central dopamine transmission in the male rat. *Brain Res.* **530**, 345–348 (1990).

27. Damsma, G., Pfaus, J. G., Wenkstern, D., Phillips, A. G. & Fibiger, H. C. Sexual behavior increases dopamine transmission in the nucleus accumbens and striatum of male rats: Comparison with novelty and locomotion. *Behav. Neurosci.* **106**, 181–191 (1992).

28. Krok, A. C. *et al.* Intrinsic dopamine and acetylcholine dynamics in the striatum of mice. *Nature* **621**, 543–549 (2023).

29. Liu, C. *et al.* An action potential initiation mechanism in distal axons for the control of dopamine release. *Science* **375**, 1378–1385 (2022).

30. Threlfell, S. *et al.* Striatal dopamine release is triggered by synchronized activity in cholinergic interneurons. *Neuron* **75**, 58–64 (2012).

31. Wang, L. *et al.* Modulation of dopamine release in the striatum by physiologically relevant levels of nicotine. *Nat. Commun.* **5**, 3925 (2014).

32. Wang, L. *et al.* Temporal components of cholinergic terminal to dopaminergic terminal transmission in dorsal striatum slices of mice. *J. Physiol.* **592**, 3559–3576 (2014).

33. Beier, K. T. *et al.* Circuit Architecture of VTA Dopamine Neurons Revealed by Systematic Input-Output Mapping. *Cell* **162**, 622–634 (2015).

34. Al-Hasani, R. *et al.* Distinct Subpopulations of Nucleus Accumbens Dynorphin Neurons Drive Aversion and Reward. *Neuron* **87**, 1063–1077 (2015).

35. Poulin, J.-F. *et al.* Mapping projections of molecularly defined dopamine neuron subtypes using intersectional genetic approaches. *Nat. Neurosci.* **21**, 1260–1271 (2018).

36. Chen, R. *et al.* Decoding molecular and cellular heterogeneity of mouse nucleus accumbens. *Nat. Neurosci.* **24**, 1757–1771 (2021).

37. Voorn, P., Gerfen, C. R. & Groenewegen, H. J. Compartmental organization of the ventral striatum of the rat: Immunohistochemical distribution of enkephalin, substance P, dopamine, and calcium-binding protein. *J. Comp. Neurol.* **289**, 189–201 (1989).

38. Cachope, R. *et al.* Selective Activation of Cholinergic Interneurons Enhances Accumbal Phasic Dopamine Release: Setting the Tone for Reward Processing. *Cell Rep.* **2**, 33–41 (2012).

39. Jones, I. W., Bolam, J. Paul. & Wonnacott, S. Presynaptic localisation of the nicotinic acetylcholine receptor β2 subunit immunoreactivity in rat nigrostriatal dopaminergic neurones. *J. Comp. Neurol.* **439**, 235–247 (2001).

40. Neve, K. A., Seamans, J. K. & Trantham-Davidson, H. Dopamine receptor signaling. *J. Recept. Signal Transduct. Res.* **24**, 165–205 (2004).

41. Greif, G. J., Lin, Y. J., Liu, J. C. & Freedman, J. E. Dopamine-modulated potassium channels on rat striatal neurons: specific activation and cellular expression. *J. Neurosci.* **15**, 4533–4544 (1995).

42. Cruz, H. G. *et al.* Bi-directional effects of GABAB receptor agonists on the mesolimbic dopamine system. *Nat. Neurosci.* **7**, 153–159 (2004).

43. Galzi, J.-L. *et al.* Mutations in the channel domain of a neuronal nicotinic receptor convert ion selectivity from cationic to anionic. *Nature* **359**, 500–505 (1992).

44. Fucile, S. Ca2+ permeability of nicotinic acetylcholine receptors. *Cell Calcium* **35**, 1–8 (2004).

45. De Mei, C., Ramos, M., Iitaka, C. & Borrelli, E. Getting specialized: presynaptic and postsynaptic dopamine D2 receptors. *Curr. Opin. Pharmacol.* **9**, 53–58 (2009).

46. Richfield, E. K., Penney, J. B. & Young, A. B. Anatomical and affinity state comparisons between dopamine D1 and D2 receptors in the rat central nervous system. *Neuroscience* **30**, 767–777 (1989).

47. Bazzett, T. J. *et al.* Dose dependent D2 effects on genital reflexes after MPOA injections of quinelorane and apomorphine. *Life Sci.* **48**, 2309–2315 (1991).

48. Lin, Y.-H. *et al.* Accumbal D2R-medium spiny neurons regulate aversive behaviors through PKA-Rap1 pathway. *Neurochem. Int.* **143**, 104935 (2021).

49. Soares-Cunha, C., Coimbra, B., Sousa, N. & Rodrigues, A. J. Reappraising striatal D1- and D2-neurons in reward and aversion. *Neurosci. Biobehav. Rev.* **68**, 370–386 (2016).

50. Raveendran, A. V. & Agarwal, A. Premature ejaculation - current concepts in the management: A narrative review. *Int. J. Reprod. Biomed.* **19**, 5–22 (2021).

51. Bronner, G., Royter, V., Korczyn, A. D. & Giladi, N. Sexual Dysfunction in Parkinson's Disease. *J. Sex Marital Ther.* **30**, 95–105 (2004).

52. Althof, S. E. *et al.* An Update of the International Society of Sexual Medicine's Guidelines for the Diagnosis and Treatment of Premature Ejaculation (PE). *Sex. Med.* **2**, 60–90 (2014).

53. Dremencov, E., Mansari, M. E. & Blier, P. Effects of sustained serotonin reuptake inhibition on the firing of dopamine neurons in the rat ventral tegmental area. *J. Psychiatry Neurosci.* **34**, 223–229 (2009).

54. Rossi, J. *et al.* Melanocortin-4-receptors Expressed by Cholinergic Neurons Regulate Energy Balance and Glucose Homeostasis. *Cell Metab.* **13**, 195–204 (2011).

55. Bäckman, C. M. *et al*. Characterization of a mouse strain expressing Cre recombinase from the 3' untranslated region of the dopamine transporter locus. *Genes. N. Y. N 2000* **44**, 383–390 (2006).

56. Lazarus, M. *et al.* Arousal effect of caffeine depends on adenosine A2A receptors in the shell of the nucleus accumbens. *J. Neurosci. Off. J. Soc. Neurosci.* **31**, 10067–10075 (2011).

57. Inoue, S. *et al.* Periodic Remodeling in a Neural Circuit Governs Timing of Female Sexual Behavior. *Cell* **179**, 1393-1408.e16 (2019).

58. Liu, C. *et al.* Posterior subthalamic nucleus (PSTh) mediates innate fear-associated hypothermia in mice. *Nat. Commun.* **12**, 2648 (2021).

59. Ishii, K. K. *et al.* A Labeled-Line Neural Circuit for Pheromone-Mediated Sexual Behaviors in Mice. *Neuron* **95**, 123-137.e8 (2017).

60. Friard, O. & Gamba, M. BORIS: a free, versatile open-source event-logging software for video/audio coding and live observations. *Methods Ecol. Evol.* **7**, 1325–1330 (2016).

61. Ting, J. T., Daigle, T. L., Chen, Q. & Feng, G. Acute brain slice methods for adult and aging animals: application of targeted patch clamp analysis and optogenetics. *Methods Mol. Biol. Clifton NJ* **1183**, 221–242 (2014).

62. Takahashi, T. M. *et al.* Optogenetic induction of hibernation-like state with modified human Opsin4 in mice. *Cell Rep. Methods* **2**, 100336 (2022).

63. Floresco, S. B., West, A. R., Ash, B., Moore, H. & Grace, A. A. Afferent modulation of dopamine neuron firing differentially regulates tonic and phasic dopamine transmission. *Nat. Neurosci.* **6**, 968–973 (2003).

64. Akiba, T., Sano, S., Yanase, T., Ohta, T. & Koyama, M. Optuna: A Next-generation Hyperparameter Optimization Framework. in *Proceedings of the 25th ACM SIGKDD International Conference on Knowledge Discovery & Data Mining* 2623–2631 (Association for Computing Machinery, 2019). doi:10.1145/3292500.3330701.

Acknowledgements

We thank M. Jing for sharing reagents; A. Yoshida, M. Endo, N. Fujii-Sekine, T. Lou, and A. Watanabe for the behavioural analysis; Editage (www.editage.com) for English language editing; K. Tanaka, N. Takata, T. Miyazaki, and H. Yamada for discussing the experiment; A. □gmo, S. Inoue, and A. Hirano for valuable discussions and comments on the manuscript. This study was supported by JSPS KAKENHI (21J2255 to A.M.), JSPS KAKENHI Grant-in-Aid for Scientific Research on Innovative Areas, "Willdynamics" (19H05006 to K.S.); AMED under Grant JP21zf0127005 (to Q.L.); the WPI program from Japan's MEXT.

Author Contributions

A.M., K.S., T.S., and Q.L. conceived the project and designed the experiments. A.M. performed all stereotaxic surgeries and conducted experiments except as noted. A.M. wrote code for photometry and optogenetics data acquisition and analyses. Y.T. performed tissue samplings. A.M. and Y.T. performed histology analyses and behavioural analyses. K.S. performed retrograde tracing. T.K., A.M., and Y.I. performed ex vivo brain slice imaging. N.N., A.M., and J.S. performed computational modelling. Y.C., A.M., and K.S. prepared AAV vectors. A.M. and T.K. performed the statistical analyses. Y.L. provided the GRAB sensors rDA2.0m and ACh3.0. A.M. and Q.L. wrote original manuscript with input from all co-authors and A.M., T.K., N.N., Y.C., M.Y., H.T., K.S., T.S., and Q.L. edited and reviewed the manuscript.

Competing interests

The authors declare that they have no competing interests.

Figure legends

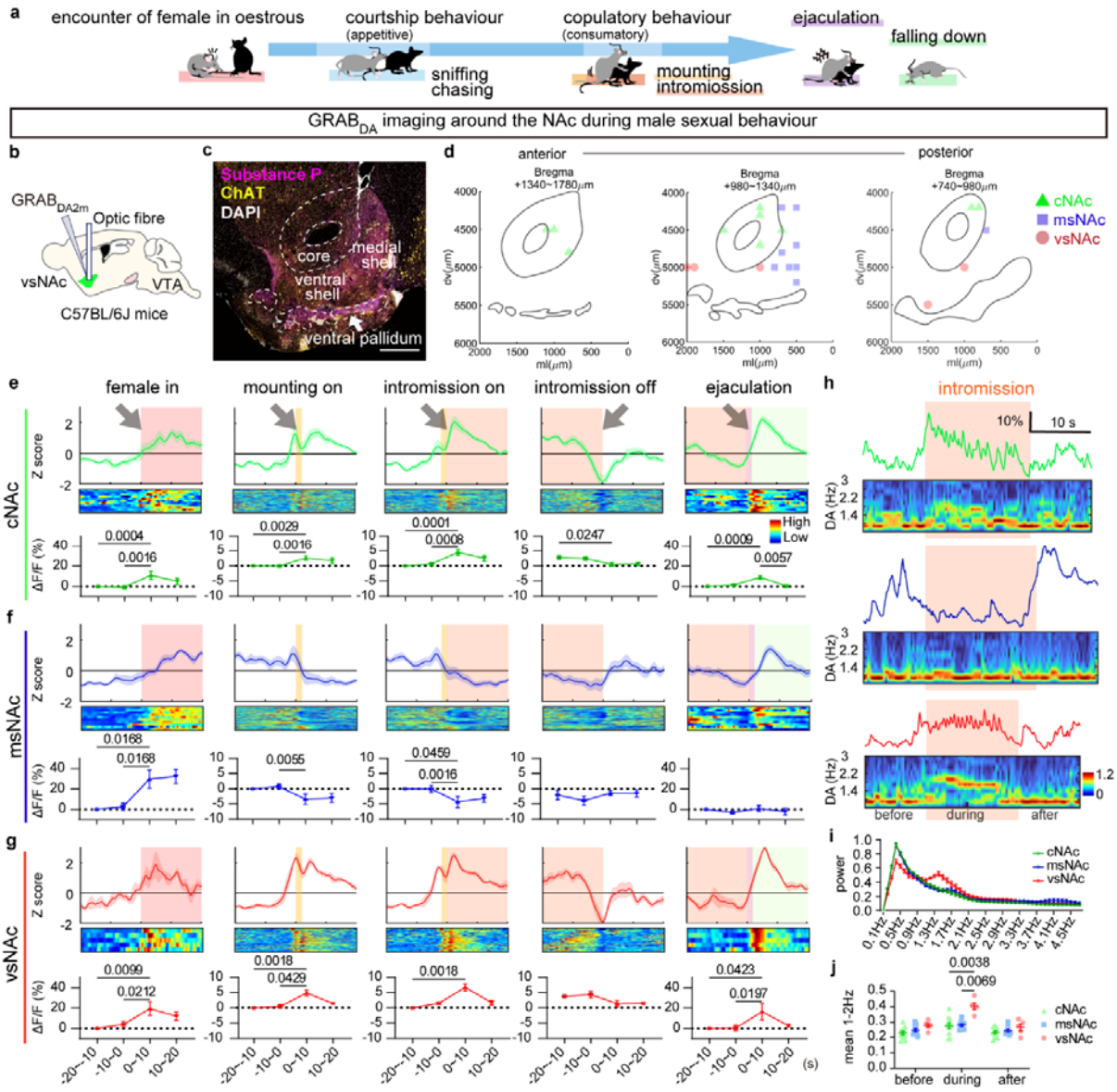

Figure 1. DA dynamics in the vsNAc closely align with serial transitions of male sexual behaviours.

a, Schematic of sexual behaviours in male mice.

b, Schematic of fibre photometry recording of GRAB$_{DA2m}$ signals in the vsNAc of C57BL/6J mice.

c, Representative image showing immunostaining of ChAT and substance P expression in the NAc and surrounding regions (scale bar = 500 μm).

d, Schematics of recording sites of GRAB$_{DA2m}$ imaging in various NAc subregions.

e-g, Top: Peri-event time plot (PETP) of z-scored ΔF/F of $GRAB_{DA2m}$ fluorescence around each transition of male sexual behaviour in the (**e**) cNAc, (**f**) msNAc, and (**g**) vsNAc. Middle: Heatmap of PETP, with individual events/row; all data from males. Bottom: Mean ΔF/F of $GRAB_{DA2m}$ of the three recording sites every 10 s in each behavioural event. See Supplementary Table 1.

h, Representative traces of $GRAB_{DA2m}$ dynamics during intromission and spectrum band calculated by FFT analysis in the (top) cNAc, (middle) msNAc, and (bottom) vsNAc.

i, Comparative power spectrum analysis of DA dynamics in the cNAc, msNAc, and vsNAc during intromission.

j, Mean power spectrum of 1–2 Hz frequency of DA dynamics before, during, and after intromission in the cNAc, msNAc, and vsNAc. See Supplementary Table 2.

Mean ± SEM n = 5 (vsNAc), 10 (msNAc), and 11 (cNAc) (**e, f, g**).

See also Extended Data Fig. 1.

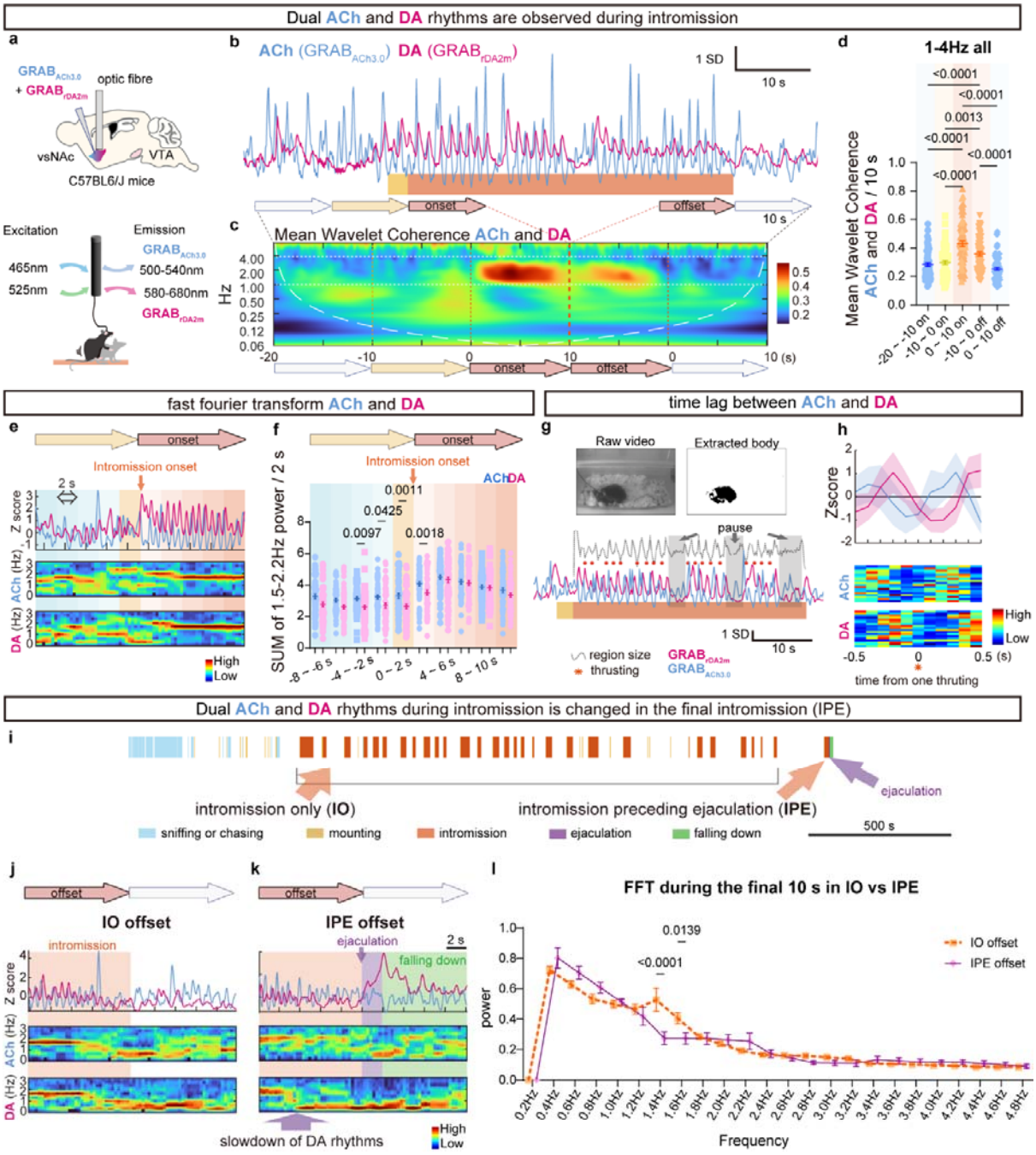

Figure 2. Dual ACh-DA rhythms are observed in the vsNAc during intromission.

a, Strategy for simultaneous fibre photometry recordings of ACh and DA dynamics in the vsNAc.

b, Representative traces of $GRAB_{ACh3.0}$ and $GRAB_{rDA2m}$ before, during, and after intromission.

c, Heatmap plot of mean wavelet coherence between $GRAB_{ACh3.0}$ and $GRAB_{rDA2m}$ dynamics around the extracted 50 s intromission.

d, Comparison of 1–4 Hz wavelet coherence between $GRAB_{Ach3.0}$ and $GRAB_{rDA2m}$ among every 10 s around intromission.

e, Representative Z-scored traces of $GRAB_{ACh3.0}$ and $GRAB_{rDA2m}$ in the vsNAc (top); heatmap showing the power spectrum processed by the FFT analysis of $GRAB_{ACh3.0}$ (centre) and $GRAB_{rDA2m}$ (bottom) around intromission onset.

f, Comparison of the total amounts of 1.5–2.2 Hz power collected every 2 s around intromission onset.

g, Thrusting was determined by the region size change of the extracted male and female mice.

h, $GRAB_{ACh3.0}$ and $GRAB_{rDA2m}$ around one thrusting during one intromission. (Top) The average traces (bottom) heatmap plot.

i, Representative laser illustration of sexual behaviour.

j, k, Same as (**e**), FFT analysis around IO offset (**j**), and IPE offset (**k**).

l, Power spectrum of $GRAB_{DA2m}$ in the vsNAc during 10 s offset of IO and IPE. Same as Fig. 1, n = 5 mice (vsNAc). Two-way ANOVA Šídák's multiple comparisons test over IO offset and IPE offset every 0.2 Hz. See Supplementary Table 6 (**d, f, l**).

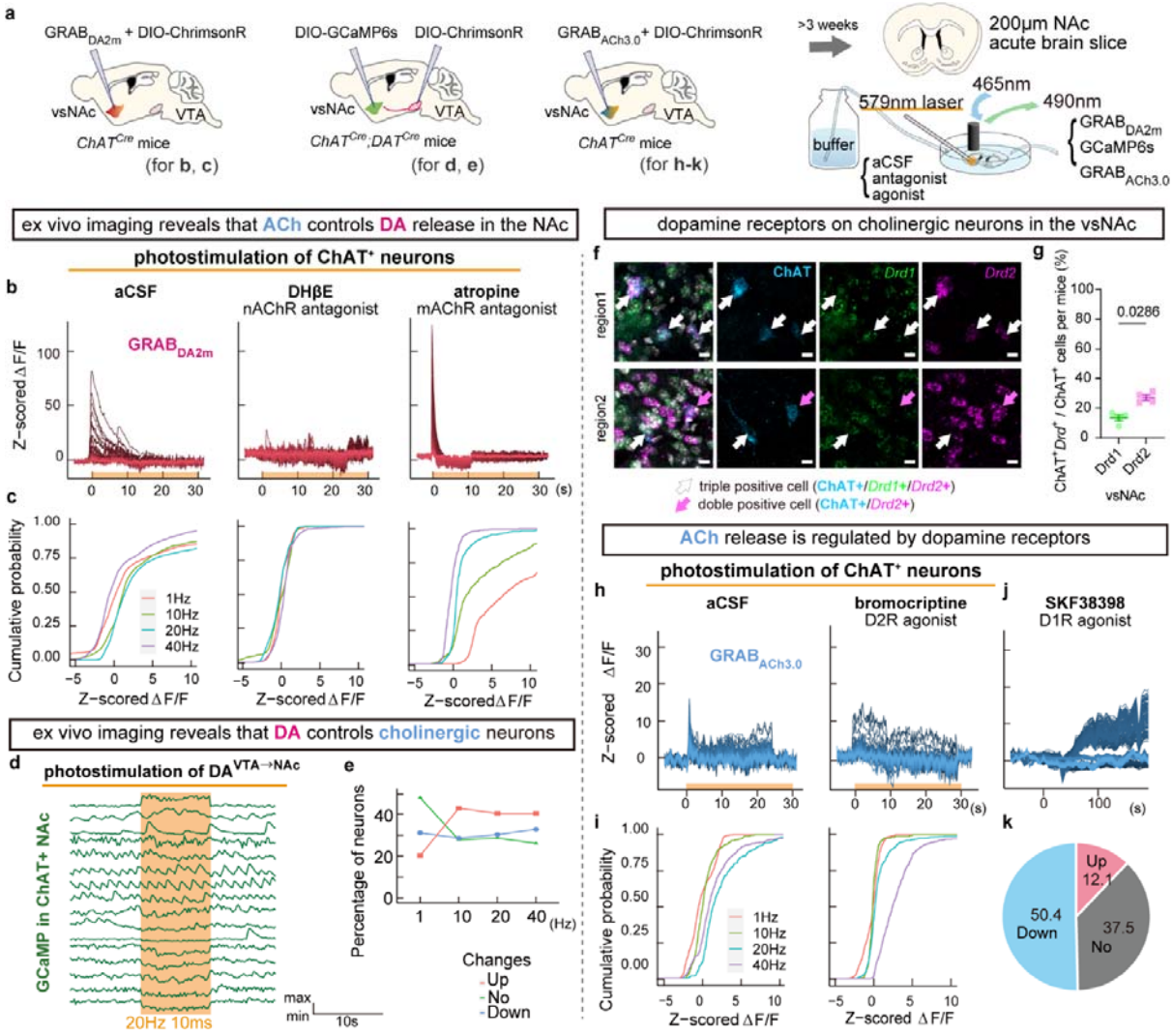

Figure 3. Ex vivo NAc brain slice imaging reveals mutual regulation of ACh and DA signalling.

a, Diagram of ex vivo experiments. Letters in parentheses indicate the corresponding figures.

b, c, Optogenetic stimulation of ChAT^{NAc} neurons and imaging of GRAB$_{DA2m}$. Representative traces of z-scored ΔF/F of GRAB$_{DA2m}$ signals in response to 10 ms-photostimulation at 20 Hz for 30 s with neither DHβE or atropine (left), with only DHβE (centre), and with only atropine (right). Bottom orange bars indicate the duration of photostimulation (**b**). Cumulative probability plots of mean z-scored ΔF/F of GRAB$_{DA2m}$ signals for 30 s after the onset of photostimulation. Plot colours indicate frequencies of the photostimulation. The experimental conditions are the same as those of

the figures directly above. n = 2332 ROIs (left), 776 ROIs (centre), and 570 ROIs (right) at any photostimulation frequency (**c**).

d, e, Optogenetic stimulation of $DA^{VTA \rightarrow NAc}$ axon terminals and Ca^{2+} imaging with GCaMP. Representative traces of GCaMP signals in response to 10 ms-photostimulation at 20 Hz for 10 s 20 Hz (**d**). Classification of $ChAT^{NAc}$ neurons by the response to photostimulation (**e**, n = 181 cells).

f, g, $ChAT^{+}$ neurons in the vsNAc are colocalised with *Drd1* and *Drd2* (scale bars = 10μm) (**f**). The ratio of $ChAT^{+}$*Drd1*$^{+}$ neurons/ $ChAT^{+}$ neurons and that of $ChAT^{+}$*Drd2*$^{+}$ neurons/ $ChAT^{+}$ neurons (**g**). See Supplementary Table 10.

h, i, Optogenetic stimulation of $ChAT^{nAc}$ neurons and imaging of $GRAB_{ACh3.0}$. Same as (**b**), but for $GRAB_{ACh3.0}$ signals in aCSF with (left) or without bromocriptine (right) (**h**). Same as (**c**), but for $GRAB_{ACh3.0}$ signals. n = 657 ROIs (1 Hz), 490 ROIs (10 Hz), 325 ROIs (20 Hz), and 654 ROIs (40 Hz) (left). N = 657 ROIs (1 Hz), 165 ROIs (10 Hz), 654 ROIs (20 Hz), and 489 ROIs (40 Hz) (right) (**i**).

j, k, Bath application of a D1R agonist and imaging of $GRAB_{ACh3.0}$. All traces of z-scored ΔF/F of $GRAB_{ACh3.0}$ signals in response to bath application of SKF38398 (**j**). Pie chart of the response pattern of the ROI (**k**, n = 685 ROIs).

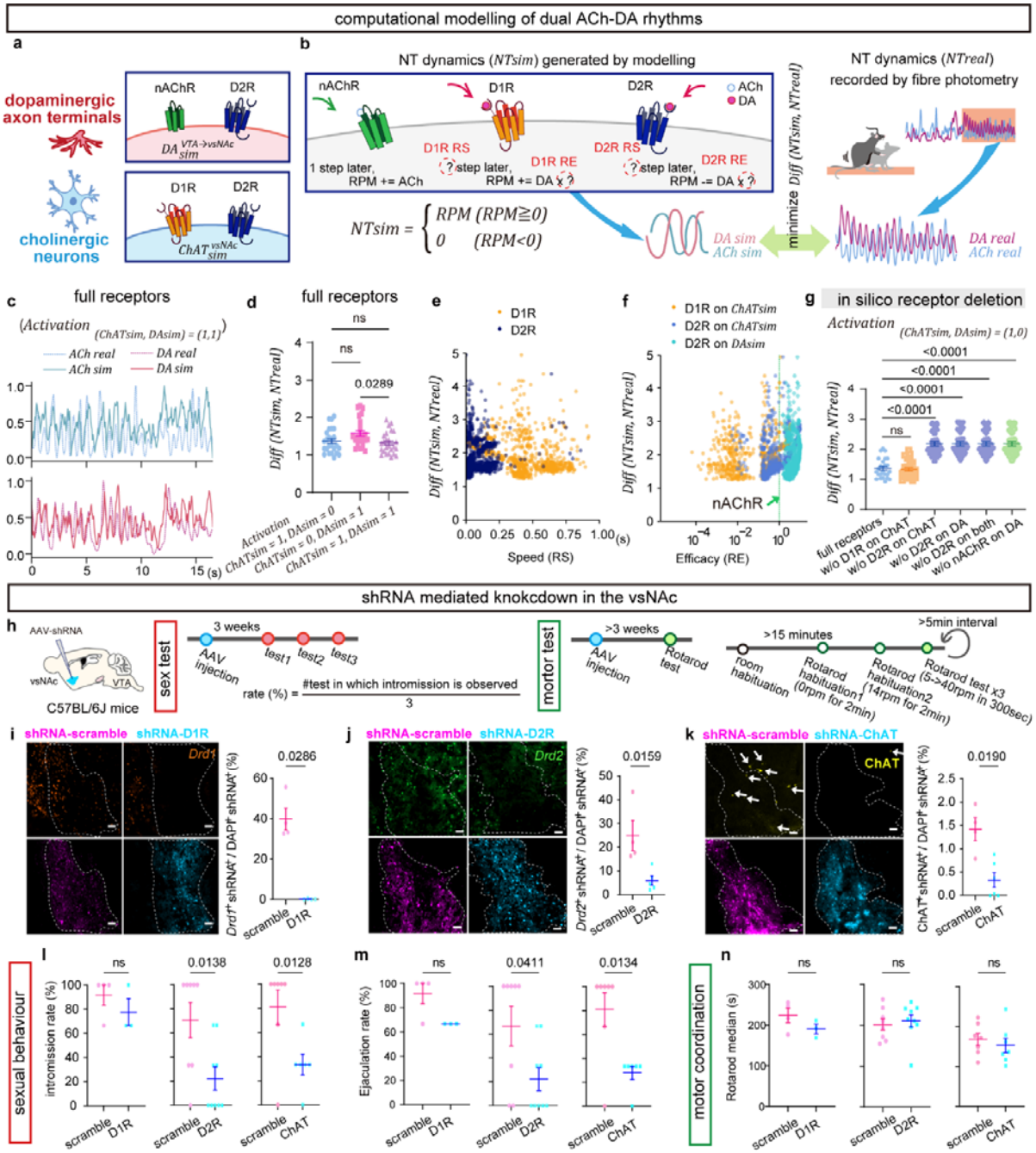

Figure 4. Computational modelling reveals that nAChR and D2R signalling are necessary for the generation of dual ACh-DA rhythms.

a, Schematic representation of the model.

b, Setting of receptors distribution in the model.

c, Representative traces of NT_{sim} and NT_{real} of ACh and DA.

d, Activation of cholinergic neurons required to generate dual ACh-DA rhythms. $Diff(NT_{sim}, NT_{real})$ for different activation input patterns with four full receptors. See Supplementary Table 11.

e, RS (Receptor speed) of D1R is larger than that of D2R in the case of generation of dual ACh-DA rhythms.

f, RE (Receptor efficacy) of D1R in $ChAT_{sim}^{vsNAc}$ is smaller than those of D2R and D2R in $ChAT_{sim}^{vsNAc}$ is smaller than D2R in $DA_{sim}^{VTA \to vsNAc}$ in the case of generation of dual ACh-DA rhythms. The RE of nAChR is shown as a green dashed line.

g, $Diff(NT_{sim}, NT_{real})$ in the condition of ablation of each receptor under the $ChAT_{sim}^{vsNAc}$:on / $DA_{sim}^{VTA \to vsNAc}$:off activation condition. See Supplementary Table 12.

Mean ± SEM data from all 59 events of 3 males.

See also Extended Data Fig. 4.

h, Schematic of gene knockdown in the vsNAc.

i-k, Coronal brain sections from shRNA targeting D1R (**i**), D2R (**j**), and ChAT (**k**) injected mice. White arrows indicate $ChAT^{+}$ cells (**k**). Scale bars = 50μm.

l, m, The effects of in vivo knockdown of D1R, D2R, or ChAT in the vsNAc on intromission rate (**l**) and ejaculation rate (**m**).

n, The effects of in vivo knockdown of D1R, D2R, or ChAT in the vsNAc on the rotarod test.

Mean ± SEM n = 4 (shRNA-scramble), 6 (shRNA-ChAT) (**k**); n = 7 (shRNA-scramble), 6 (shRNA-ChAT) (**l, m**); n = 7 (shRNA-scramble), 7 (shRNA-ChAT) (**n**); n = 4 (shRNA-scramble), 3 (shRNA-D1R) (**i, l-n**); n = 4 (shRNA-scramble), 5 (shRNA-D2R) (**j**); n = 8 (shRNA-scramble), 9 (shRNA-D2R) (**l, m**); n = 8 (shRNA-scramble), 9 (shRNA-ChAT) (**n**).

$*p < 0.05$, $**p < 0.01$, $***p < 0.001$.

See also Extended Data Fig. 5 and Supplementary Table 13-16.

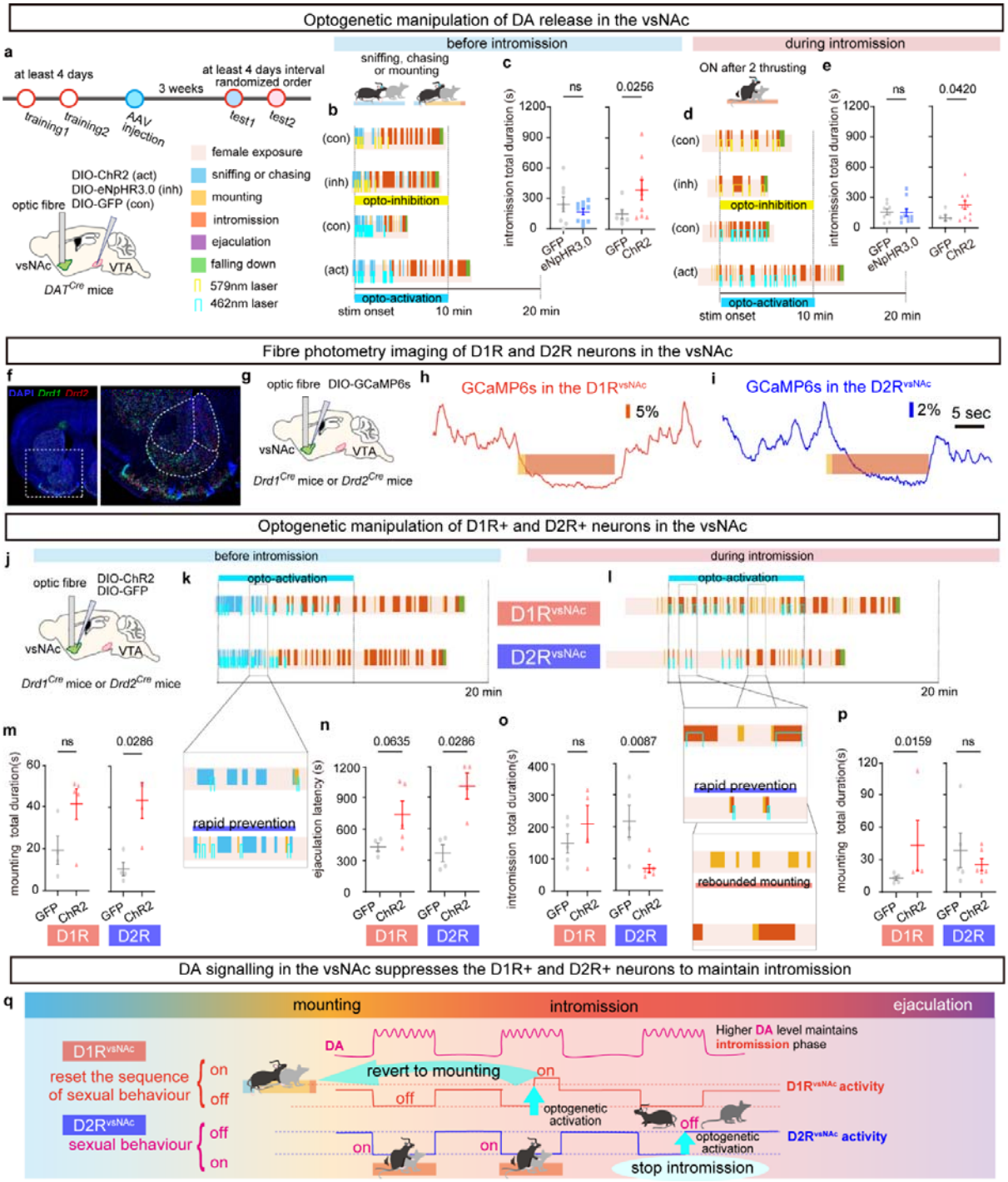

Figure 5. Activation of DA release into vsNAc increases intromission behaviour.

a, Strategy for optogenetic manipulation. Experimental schedule (top) and surgery design (bottom). **b**, **d**, Laser illustration of sexual behaviour and optogenetic manipulation before intromission (**b**) and during intromission (**d**).

c, **e**, The effect of the optogenetic inhibition (left) and activation (right) of DA release into the vsNAc before (**c**) and during (**e**) intromission on the intromission total duration.

Mean ± SEM n = 8 (GFP, control for eNpHR3.0), 10 (eNpHR3.0), n = 6 (GFP, control for ChR2), 9 (ChR2) (**c**); n = 8 (GFP, control for eNpHR3.0), 10 (eNpHR3.0), n = 6 (GFP, control for ChR2) 10 (ChR2) (**e**). $*p < 0.05$.

See also Extended Data Fig. 6 and Supplementary Table 17, 18.

f, in situ staining of *Drd1* and *Drd2* around the NAc.

g, Schematic of fibre photometry recording of GCaMP6s signals expressed in the D1R or D2R-expressing neurons in the vsNAc of $Drd1^{Cre}$ or $Drd2^{Cre}$ mice, respectively.

h, **i**, Neuronal activity of $D1R^{vsNAc}$ (**h**) and $D2R^{vsNAc}$ neurons (**i**) are suppressed during intromission.

See also Extended Data Fig. 7a, b and Supplementary Table 19, 20.

j, Strategy for optogenetic manipulation of $D1R^{vsNAc}$ and $D2R^{vsNAc}$ neurons. See Extended Data Fig.7.

k, **l**, Laser illustration of sexual behaviour and optogenetic manipulation of $D1R^{vsNAc}$ and $D2R^{vsNAc}$ neurons before (**k**) and during intromission (**l**).

m, **n**, The effect of the optogenetic activation of $D1R^{vsNAc}$ (left) and $D2R^{vsNAc}$ neurons (right) before intromission on the mounting total duration (**m**) and ejaculation latency (**n**).

o, **p**, The effect of the optogenetic activation of $D1R^{vsNAc}$ (left) and $D2R^{vsNAc}$ neurons (right) during intromission on the intromission total duration (**o**) and mounting total duration (**p**).

q, Suppressed $D1R^{vsNAc}$ and $D2R^{vsNAc}$ during intromission is important for the forwarding the sexual behaviour.

Mean ± SEM n = 5 (GFP in $D1R^{vsNAc}$), 4 (ChR2 in $D1R^{vsNAc}$), n = 4 (GFP in $D2R^{vsNAc}$), 4 (ChR2 in $D2R^{vsNAc}$) (**m, n**); n = 4 (GFP in $D1R^{vsNAc}$), 5 (ChR2 in $D1R^{vsNAc}$), n = 5 (GFP in $D2R^{vsNAc}$), 6 (ChR2 in $D2R^{vsNAc}$) (**o, p**). $*p < 0.05$, $**p < 0.01$.

See also Extended Data Fig. 7c-f; Supplementary Table 21, 22.

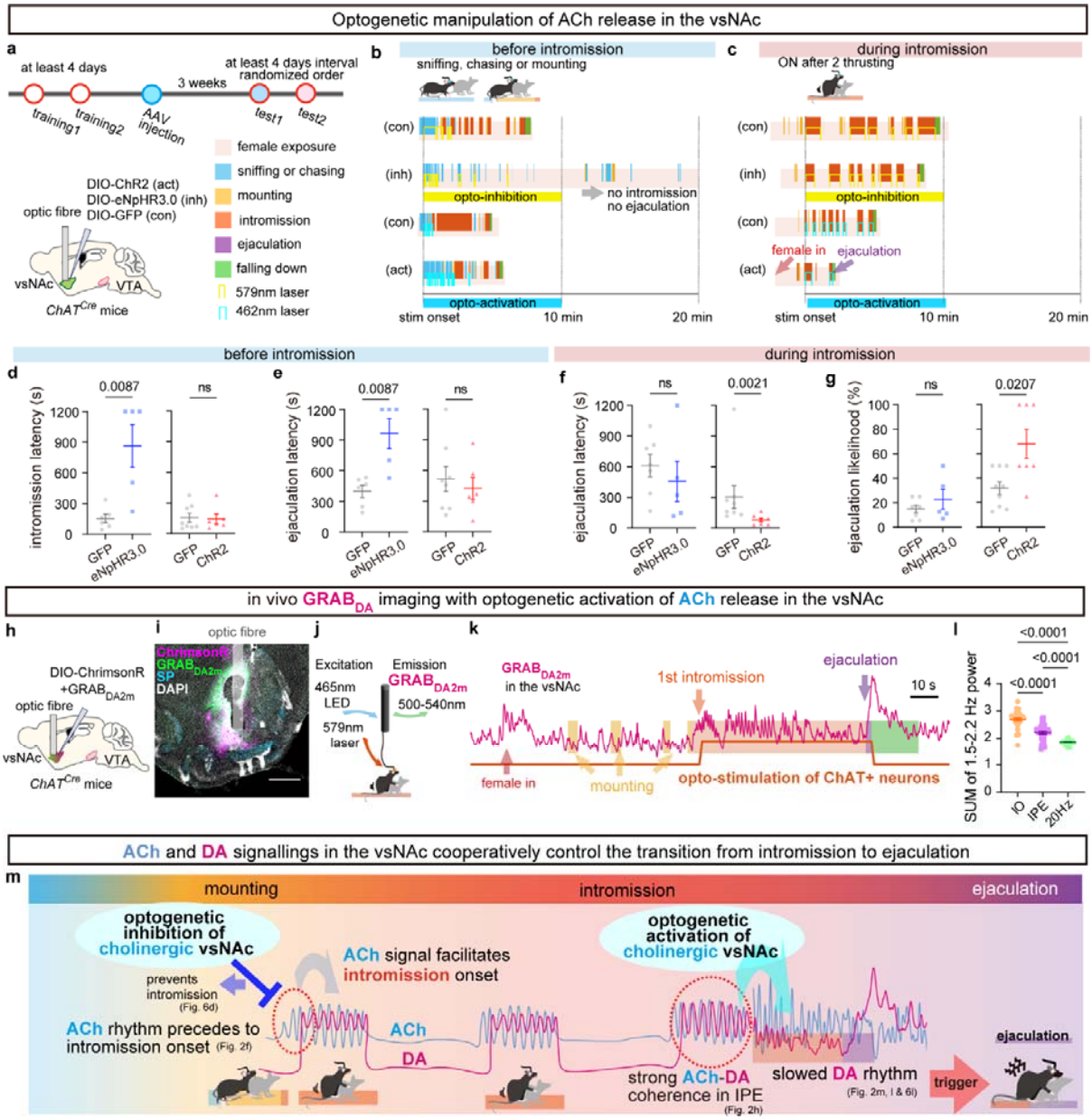

Figure 6. Optogenetic activation of ACh release into vsNAc during intromission induces ejaculation by triggering slowdown of Da rhythm.

a, Strategy for optogenetic manipulation. Experimental schedule (top) and surgery design (bottom).

b, **c**, Laser illustration of sexual behaviour and optogenetic manipulation before intromission (**b**) and during intromission (**c**).

d, **e**, The effect of the optogenetic inhibition (left) and activation (right) of $ChAT^{vsNAc}$ neurons before intromission on the intromission latency (**d**) and ejaculation latency (**e**).

f, **g**, The effect of the optogenetic inhibition (left) and activation (right) of $ChAT^{vsNAc}$ neurons during intromission on the ejaculation latency (**f**) and ejaculation likelihood (**g**).

Mean ± SEM n = 6 (GFP, control for eNpHR3.0), 5 (eNpHR3.0), n = 8 (GFP, control for ChR2), 6 (ChR2) (**d, e**); n = 7 (GFP, control for eNpHR3.0), 5 (eNpHR3.0), n = 9 (GFP, control for ChR2), 7 (ChR2)) (**f, g**). $*p < 0.05$, $**p < 0.01$.

h-l, Activation of $ChAT^{vsNAc}$ neurons induces a slowdown of the DA rhythm.

m, ACh rhythm appears before intromission, while the optogenetic inhibition of $ChAT^{vsNAc}$ neurons before intromission may prevent these ACh rhythms and the intromission onset. The optogenetic activation of $ChAT^{vsNAc}$ neurons during intromission may mimic the increased coherence of ACh and DA and that ACh precedes DA more in IPE than in IO, which may trigger a slowdown of DA rhythm and ejaculation.

See also Extended Data Fig. 8, Supplementary Table 23-25.

Extended Data Figures

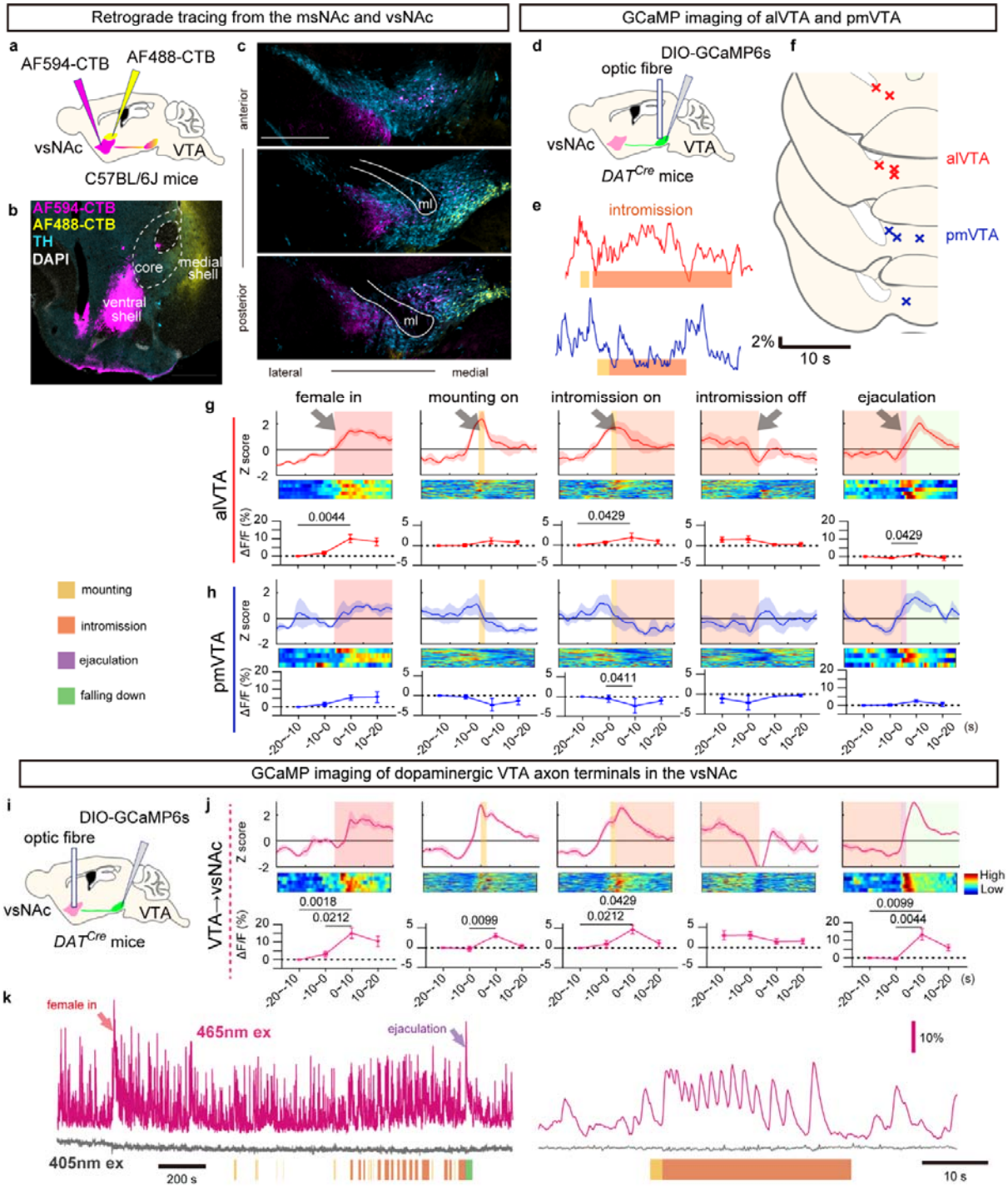

Extended Data Fig. 1. Rhythmic neuronal activity of dopaminergic neurons is observed only in axon terminals in vsNAc (related to Figure 1).

a-c, The anterior-lateral VTA projects to the vsNAc, while the posterior-medial VTA projects to the msNAc (scale bars = 500 μm).

d-h, The neuronal activity of dopaminergic neurons in VTA subregions correspond to the projection sites in NAc but did not fluctuate during intromission. See Supplementary Table 3.

d, Recording sites of GCaMP6s imaging in the VTA of *DAT*^{Cre} mice: alVTA and pmVTA. € Strategy for imaging of GCaMP6s around the VTA subregions in *DAT*^{Cre} mice.

e, Representative traces for ΔF/F of GCaMP6s around the VTA subregions during intromission with laser illustration of sexual behaviour.

f, PETP of GCaMP6s fluorescence at each recording site around each sexual behaviour.

g, h, The neuronal activity of dopaminergic axon terminals in vsNAc shows rhythmic fluctuation during intromission.

i, Strategy for imaging of GCaMP6s of the axon terminals of VTA in vsNAc of *DAT*^{Cre} mice.

j, PETP of GCaMP6s fluorescence of dopaminergic axon terminals in vsNAc around each sexual behaviour. See Supplementary Table 4.

k, Representative traces for ΔF/F of GCaMP6s excited by 465 nm (Ca^{2+} dependent) and 405 nm (Ca^{2+} independent) LED around the VTA subregions during intromission with laser illustration of sexual behaviour.

Mean ± SEM n = 5 (alVTA), 4 (pmVTA) (**d-h**); n = 5 (VTA→vsNAc) (**i-k**).

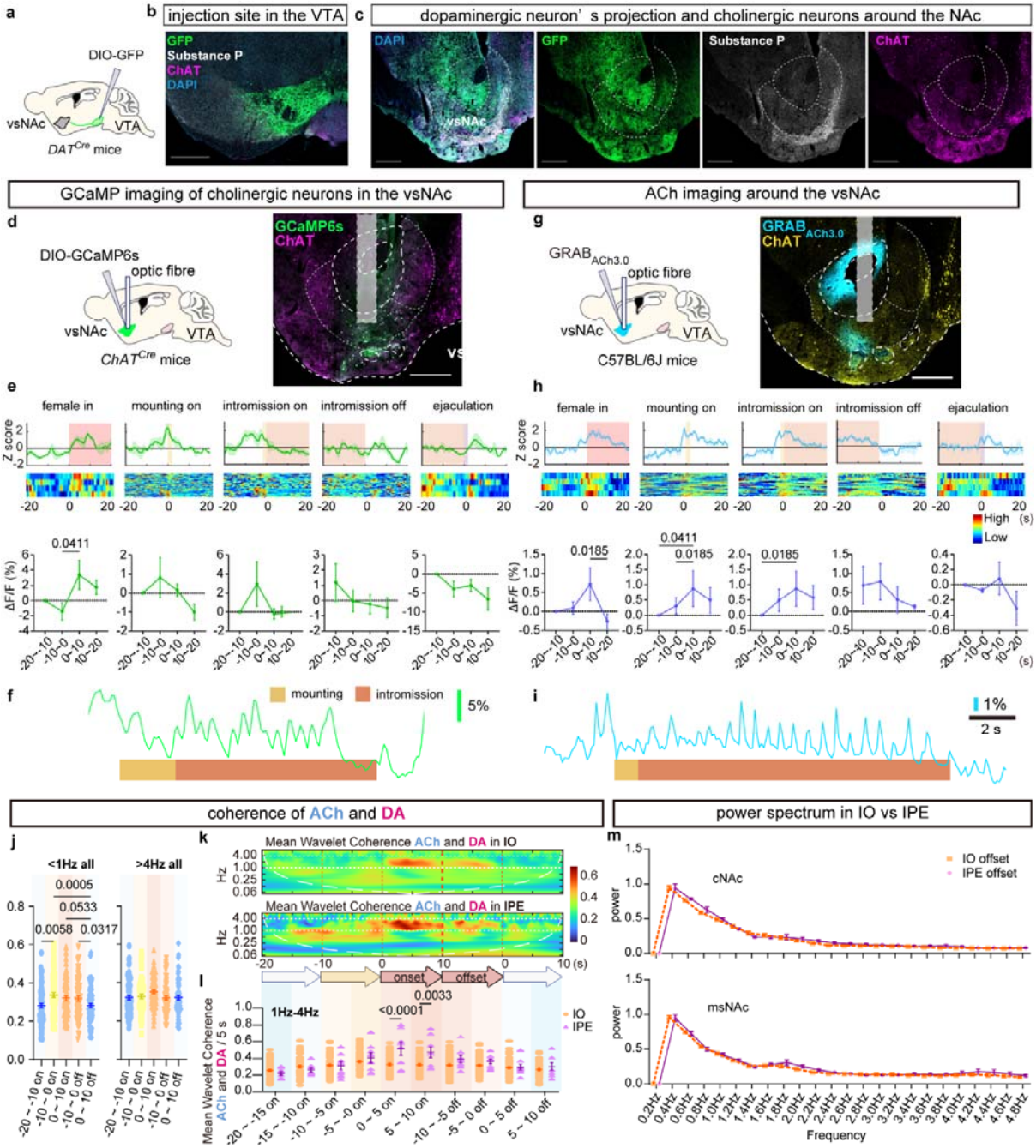

Extended Data Fig. *2.* **ACh dynamics and neuronal activity of cholinergic interneurons are rhythmic during intromission (related to Figure 2).**

a-c, Dopaminergic axons project to the vsNAc and cholinergic interneurons in the vsNAc (scale bar = 500 μm). Strategy for labelling of dopaminergic neurons using AAV (**a**). Immunostained coronal brain sections for GFP, ChAT, substance P, and DAPI around the VTA (**b**) and NAc (**c**).

d-f, The neuronal activity of cholinergic neurons in vsNAc is rhythmic during intromission.

g-i, ACh release into vsNAc is rhythmic during intromission.

(**d, g**) Strategy for imaging of GCaMP6s in cholinergic neurons in the vsNAc in *ChAT*^{Cre} mice (**d**) and $GRAB_{ACh3.0}$ in the vsNAc in C57BL/6J mice (**g**). Coronal brain sections for GCaMP6s (**d**) and $GRAB_{ACh3.0}$ (**g**) immunostained for ChAT (scale bars = 500 μm).

(**e, h**) PETP of GCaMP6s (**e**) and $GRAB_{ACh3.0}$ (**h**) fluorescence at each recording site around each sexual behaviour. See also Supplementary Table 5.

(**f, i**) Representative traces for ΔF/F of GCaMP6s (**f**) and $GRAB_{ACh3.0}$ (**i**) during intromission with laser illustration of sexual behaviour.

Mean ± SEM n = 5 (**d-f**); n = 4 (**g-i**).

j, Mean wavelet coherence between $GRAB_{ACh3.0}$ and $GRAB_{rDA2m}$ every 10 s around intromission of <1Hz IO (left) and >4Hz IO (right).

k, Heatmap plot of mean wavelet coherence between $GRAB_{ACh3.0}$ and $GRAB_{rDA2m}$ around IO (top) and IPE (bottom).

l, Comparison of 1–4 Hz wavelet coherence between $GRAB_{ACh3.0}$ and $GRAB_{rDA2m}$ every 10 s around intromission among IO and IPE. See Supplementary Table 7.

m, Power spectrum of $GRAB_{DA2m}$ in the cNAc (top) and msNAc (bottom) during 10 s offset of IO and IPE. n = 10 mice (cNAc), n = 9 mice (msNA). Two-way ANOVA Šídák's multiple comparisons test over IO offset and IPE offset every 0.2 Hz. *ns* in all frequency in the cNAc and msNAc. See Supplementary Table 8.

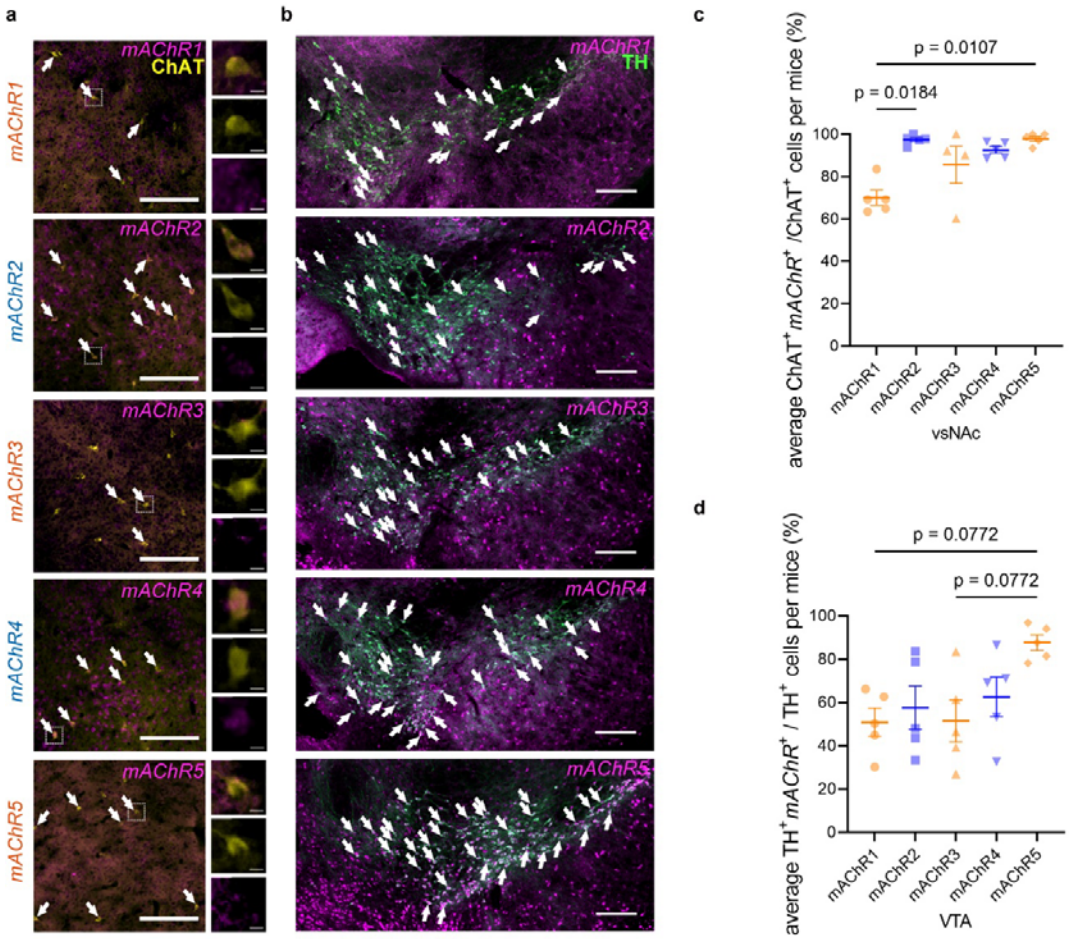

Extended Data Fig. 3. *mAChR1-5* on cholinergic neurons in the vsNAc and on dopaminergic neurons in the VTA (related to Figure 3).

a, Coronal brain sections around the NAc stained with anti-ChAT and in situ hybridisation of *mAChR* subtype1–5 (*mAChR1*, *mAChR2*, *mAChR3*, *mAChR4*, and *mAChR5* represent *Chrm1*, *Chrm2*, *Chrm3*, *Chrm4*, and *Chrm5*, respectively). Scale bars = 200 µm (left). Enlarged images of white squares surrounding areas in left images (scale bars = 10 µm) (right).

b, Coronal brain sections around the VTA stained with anti-TH and in situ hybridisation of *mAChR* subtypes 1–5 (scale bars = 200 µm). White arrows indicate the double positive cells such as *mAChR1*$^{+}$ChAT^{+} cells (**a**, **b**).

c, The ratio of ChAT^{+} cells expressing each *mAChR* subtype to the total number of ChAT^{+} cells in the vsNAc (%).

d, The ratio of TH^+ cells expressing each *mAChR* subtype to the total number of TH^+ cells in the VTA (%).

Mean ± SEM n = 5 in *mAChR1,2,4,5* and n = 4 in *mAChR3* (**a**, **c**); n = 5 in each *mAChR* (**b**, **d**). See also Supplementary Table 9.

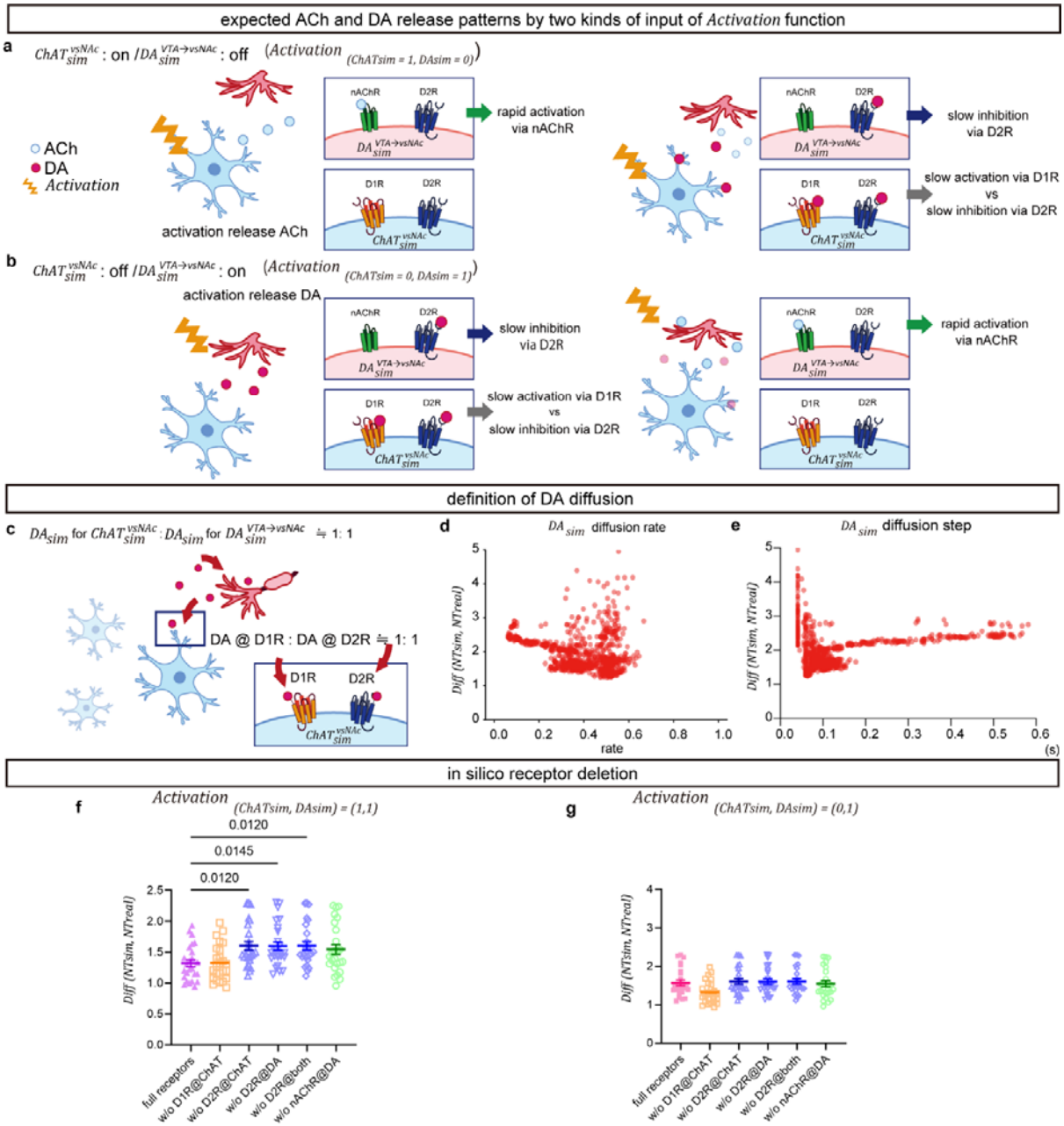

Extended Data Fig. 4. Modelling explored activation pattern of each neuron (related to Figure 4).

a, b, The expected release patterns of ACh and DA depend on the different activation inputs on (**a**) $ChAT_{sim}^{vsNAc}$ ($Activation_{(1,0)}$), and (**b**) $DA_{sim}^{VTA\rightarrow vsNAc}$ ($Activation_{(0,1)}$).

c, Distribution setting of released DA_{sim} toward D1R and D2R on $ChAT_{sim}^{vsNAc}$ neurons and D2R on $DA_{sim}^{VTA\rightarrow vsNAc}$ axon terminals (D1R on $ChAT_{sim}^{vsNAc}$: D2R on $ChAT_{sim}^{vsNAc}$: D2R on $DA_{sim}^{VTA\rightarrow vsNAc}$=1:1:2).

d, Relationship between $Diff(NT_{sim}, NT_{real})$ and explored DA diffusion rate.

e, Relationship between $Diff(NT_{sim}, NT_{real})$ and the explored DA diffusion step.

f, g, $Diff(NT_{sim}, NT_{real})$ in the condition of ablation of each receptor in the condition of (**f**) $Activation_{(1,1)}$ and (**g**) $Activation_{(0,1)}$. For (**f**) and (**g**), the Kruskal–Wallis test was used for statistical analysis, and data are shown as the mean ± SEM. See Supplementary Table 12.

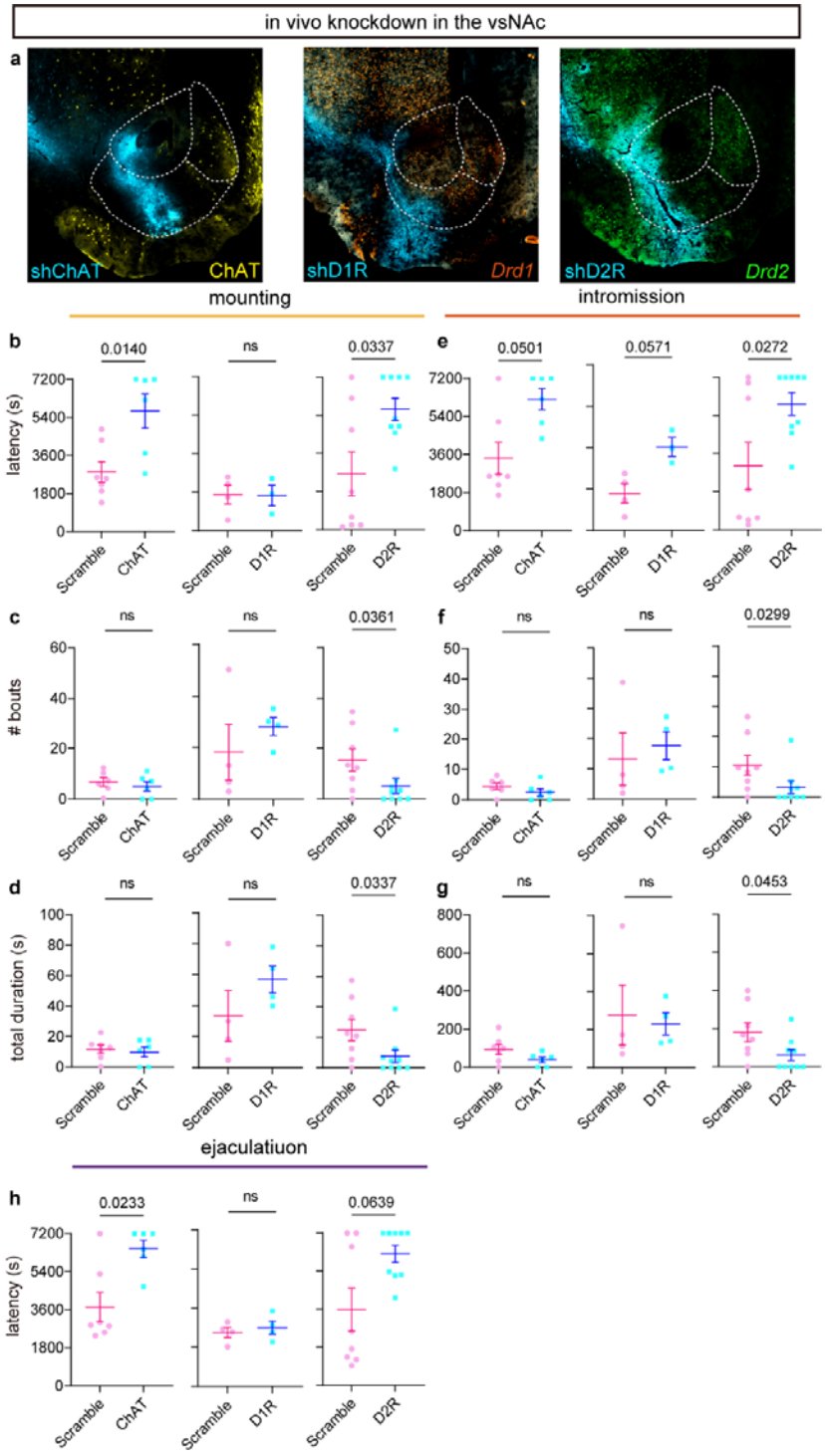

1381

1382 **Extended Data Fig. 5. Gene knockdown of ChAT, D1R, and D2R in the vsNAc (related to**

1383 **Figure 4).**

1384 **a,** The AAV-shRNA is injected into the vsNAc.

b-h, The results of gene knockdown of ChAT (left), D1R (centre) and D2R (right). (**b-d**) The knockdown effects on mounting behaviour, its latency (**b**), its number of bouts (**c**), and its total duration (**d**). (**e-g**) The knockdown effects on intromission behaviour, its latency (**e**), its number of the bout (**f**), and its total duration (**g**). (**h**) The knockdown effect on ejaculation.

See also Supplementary Table 15.

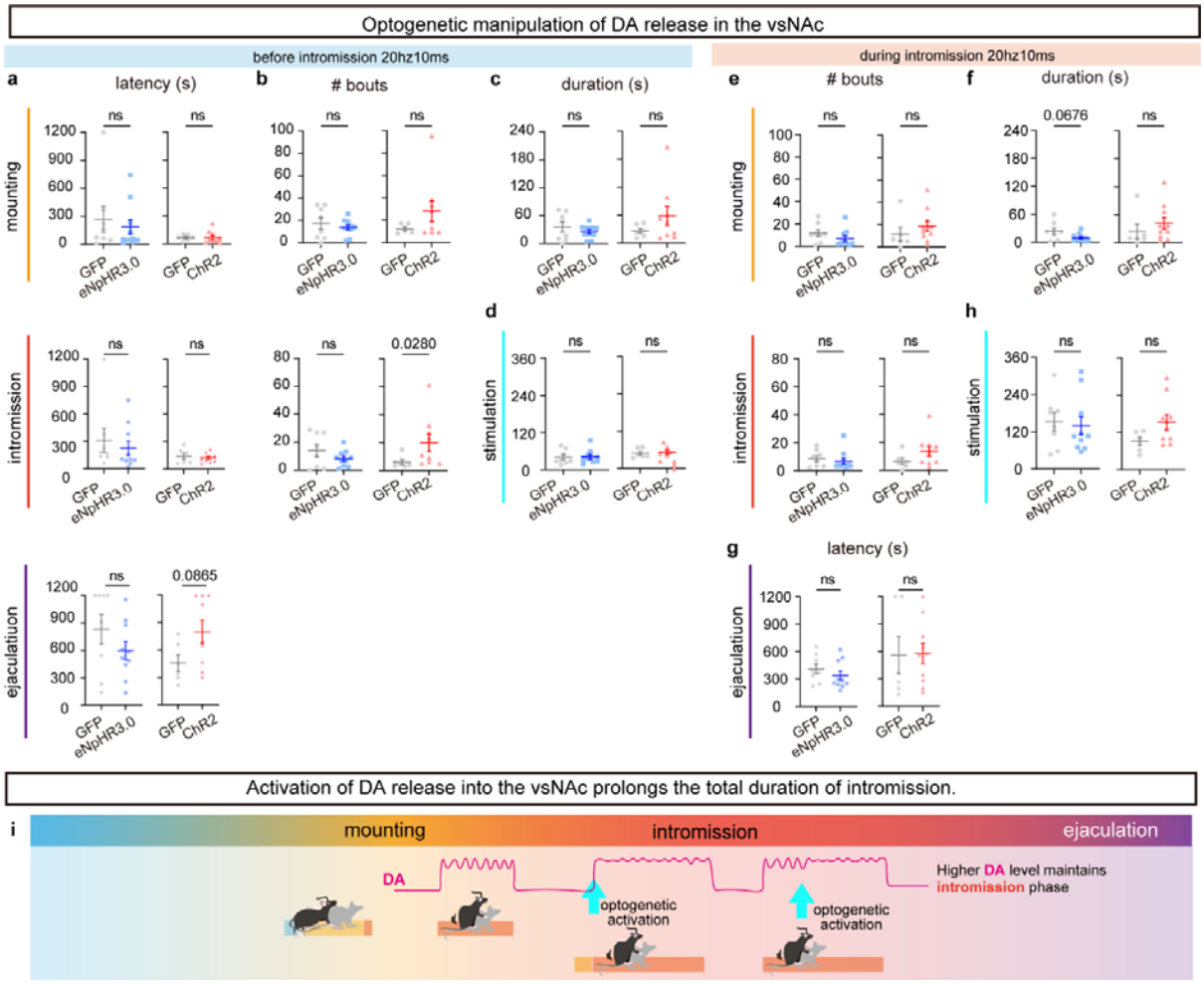

Extended Data Fig. 6. Optogenetic manipulation of dopaminergic axons in the vsNAc around intromission (related to Figure 5).

a-h, The effects of optogenetic inhibitory (left, eNpHR3.0) and excitatory (right, ChR2) manipulation of $DA^{VTA \rightarrow vsNAc}$ axons before intromission (**a-d**) and during intromission (**e-h**).

a-d, Activation of $DA^{VTA \rightarrow vsNAc}$ axons before intromission increases the number of intromission bouts, while inhibition does not affect sexual behaviour. The duration of optogenetic stimulation is not different depending on each group.

e-h, Manipulation of $DA^{VTA \rightarrow vsNAc}$ axons during intromission does not affect sexual behaviour. The duration of optogenetic stimulation is not different depending on each group.

i, Optogenetic activation of $DA^{VTA \rightarrow vsNAc}$ axons either before or during intromission increases intromission behaviour, while inhibition does not affect the sexual behaviour.

See also Supplementary Table 17, 18.

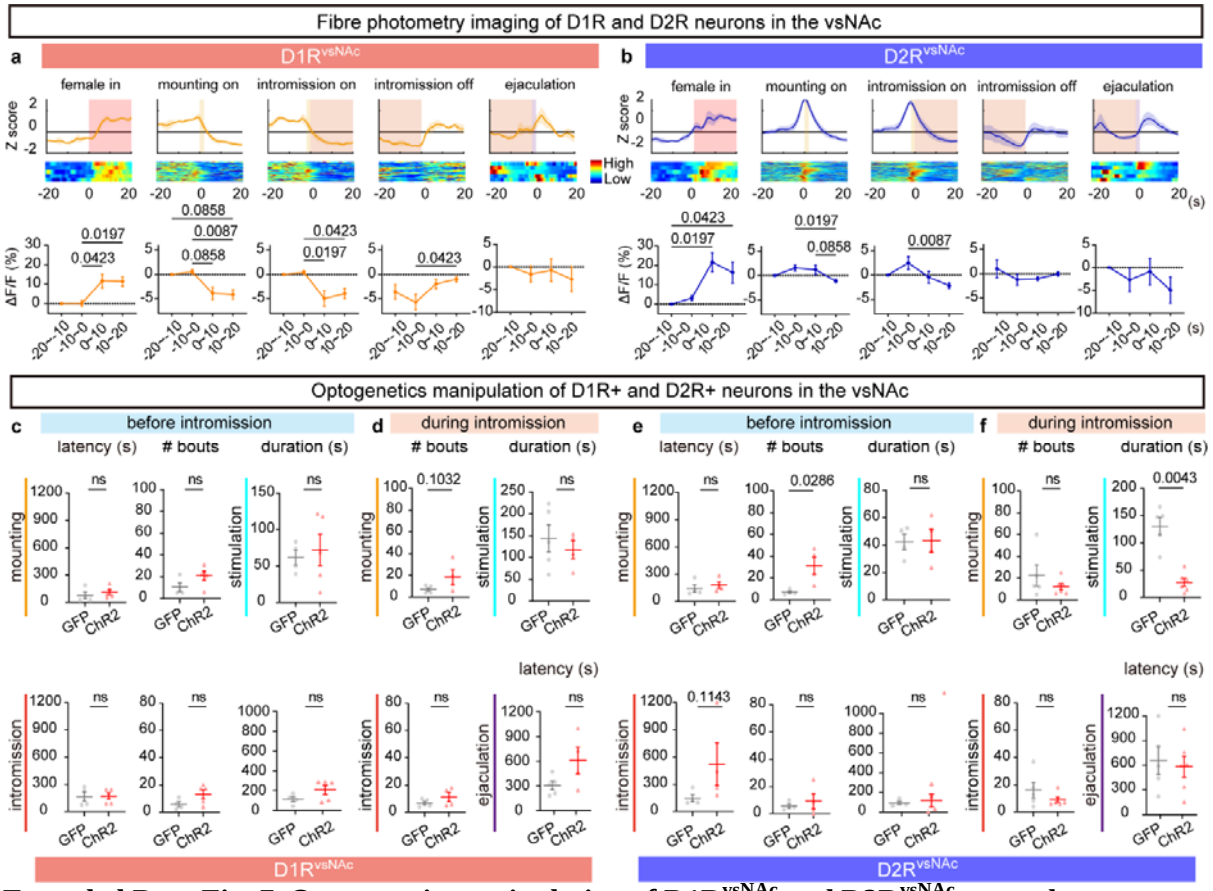

Extended Data Fig. 7. Optogenetic manipulation of D1R^{vsNAc} and D2R^{vsNAc} around intromission (related to Figure 5).

a, b, PETP of GCaMP fluorescence at D1R^{vsNAc} (**a**) and D2R^{vsNAc} (**b**) around each sexual behaviour.

c-f, The effects of optogenetic excitatory (ChR2) manipulation of D1R^{vsNAc} (**c, d**) and D2R^{vsNAc} (**e, f**) before intromission (**c, e**) and during intromission (**d, f**).

Mean ± SEM n = 5 (**a**); n = 5 (**b**). See Supplementary Table 19, 20.

Mean ± SEM n = 5 (GFP in D1R^{vsNAc}), 4 (ChR2 in D1R^{vsNAc}) (**c**); n = 4 (GFP in D1R^{vsNAc}), 5 (ChR2 in D1R^{vsNAc}) (**d**); n = 4 (GFP in D2R^{vsNAc}), 4 (ChR2 in D2R^{vsNAc}) (**e**); n = 5 (GFP in D2R^{vsNAc}), 6 (ChR2 in D2R^{vsNAc}) (**f**). $^{*}p < 0.05$, $^{**}p < 0.01$.

See Supplementary Table 21, 22.

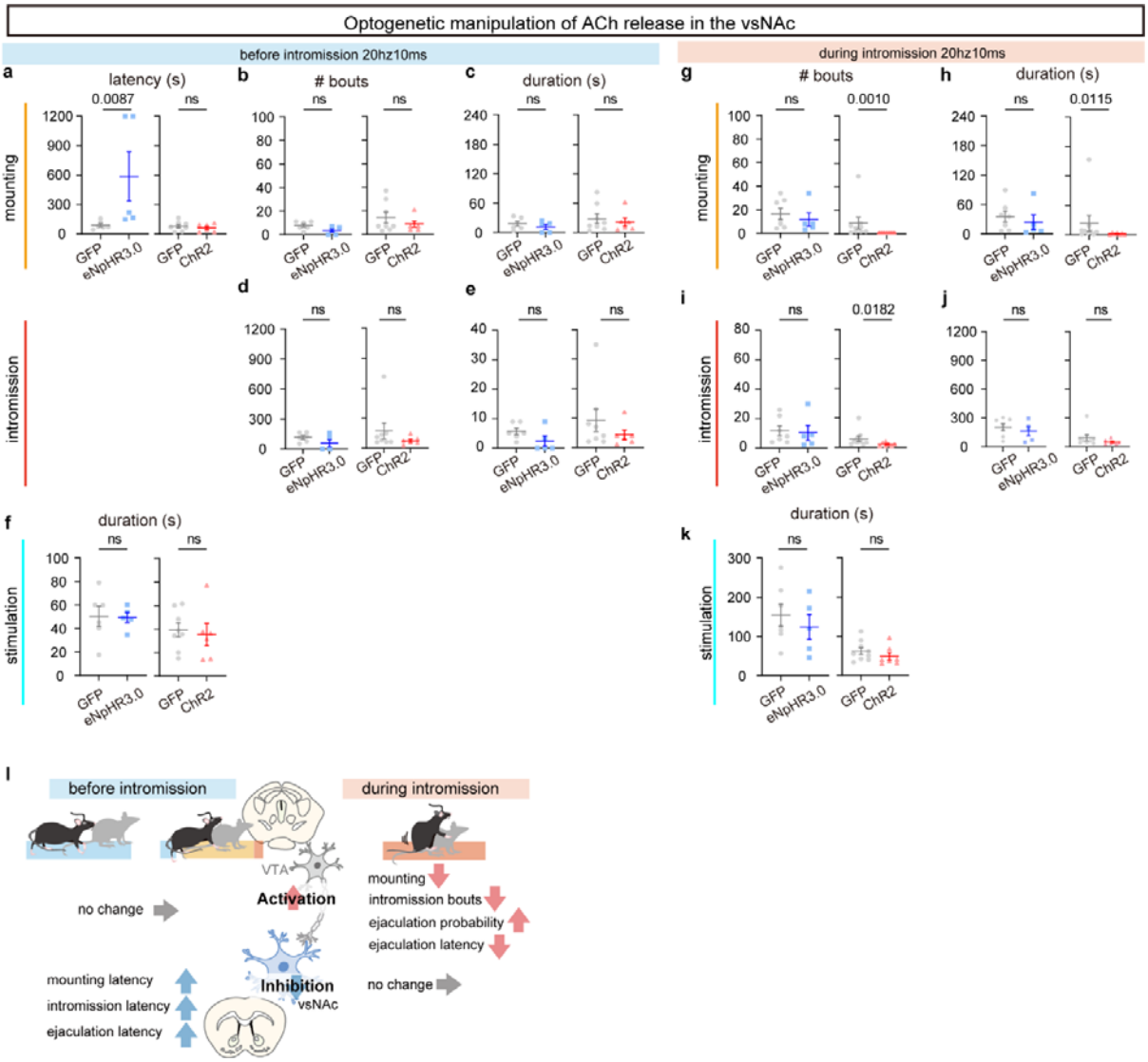

Extended Data Fig. 8. Optogenetic manipulation of cholinergic neurons in the vsNAc around intromission (related to Figure 6).

a-k, The effects of optogenetic inhibitory (left, eNpHR3.0) and excitatory (right, ChR2) manipulation of ChAT^{vsNAc} neurons before intromission (**a-f**) and during intromission (**g-k**).

a-f, Inhibition of ChAT^{vsNAc} neurons before intromission prolongs the latency of mounting behaviour (**a**), while inhibition does not affect the sexual behaviour (**a-g**). The duration of optogenetic stimulation is not different depending on each group (**f**).

g-k, Activation of ChAT^{vsNAc} neurons during intromission decreases the number of mounting bouts (**g**), intromission bouts (**i**) and the total duration of mounting (**h**), while inhibition does not affect

sexual behaviour (**g-j**). The duration of optogenetic stimulation is not different depending on each group (**k**).

l, Optogenetic activation of $ChAT^{vsNAc}$ neurons before intromission does not affect sexual behaviour, while inhibition increases the latency of mounting, intromission, and ejaculation. Optogenetic activation of $ChAT^{vsNAc}$ neurons during intromission decreases mounting, the number of intromission bouts, and ejaculation latency, and increases ejaculation probability which the optogenetic manipulation induces ejaculation.

See Supplementary Table 23, 24.